Transparent materials based on semiconducting ZnO: glass-ceramics and optical ceramics doped with rare-earth and transition-metal ions

Olga Dymshits[1], Elena Gorokhova[1], Irina Alekseeva[1], Valery Golubkov[2], Michael Shepilov[1], Alexander Khubetsov[1], Marina Tsenter[1], Daria Shemchuk[1], Anastasiya Bachina[1], Anna Volokitina[3], Lisa Basyrova[4], Michail Baranov[3], Eugenia Oreschenko[1], Xavier Mateos[5,6], Pavel Loiko[4], Aleksandr Zhilin[7]

[1] *S.I. Vavilov State Optical Institute, 36 Babushkina St., 192171, St. Petersburg, Russia*
[2] *Institute of Silicate Chemistry of Russian Academy of Sciences, Adm. Makarova emb., 2, St. Petersburg, 199034, Russia*
[3] *ITMO University, Kronverksky Pr. 49, St. Petersburg, 197101, Russia*
[4] *Centre de Recherche sur les Ions, les Matériaux et la Photonique (CIMAP), UMR 6252 CEA-CNRS-ENSICAEN, Université de Caen Normandie, 6 Boulevard Maréchal Juin, 14050 Caen Cedex 4, France*
[5] *Universitat Rovira i Virgili (URV), Física i Cristal·lografia de Materials i Nanomaterials (FiCMA-FiCNA), Marcel·lí Domingo 1, 43007, Tarragona, Spain*
[6] *Serra Húnter Fellow, Spain*
[7] *D.V. Efremov Institute of Electrophysical Apparatus, 196641, St. Petersburg, Russia*

Abstract

The structure of ZnO based transparent glass-ceramics prepared from glasses by controlled crystallization and of optical ceramics prepared by uniaxial recrystallization hot pressing and doped with rare-earth (RE) and transition metal (TM) ions are compared.

Regions of structural inhomogeneity are formed in glasses during their casting, cooling and annealing. Their composition depends on the type and concentration of TM and RE ions and determines the difference in phase assemblage of glass-ceramics. In optical ceramics, RE ions do not enter the structure of ZnO crystals, but are located on their surface and form the RE_2O_3 phase. The RE_2O_3 fraction increases proportionally to the RE ion doping level. ZnO glass-ceramics and optical ceramics doped with TM and RE ions are multiphase materials.

Keywords: crystallization; ZnO; glass-ceramics; ceramics; rare-earth ions; transition metal ions

1. Introduction

Zinc oxide powders, films, single crystals, ceramics and glass-ceramics, either undoped or doped with transition metal (TM) and rare-earth (RE) ions, are among the most actively studied materials [1-5]. This is due to the unique combination of their physical and chemical properties, such as a wide bandgap (3.37 eV), large exciton binding energy of 60 meV, high chemical, thermal and mechanical stability, low toxicity, biocompatibility and biodegradability. Moreover, the properties of ZnO materials are tunable. Zinc oxide is an efficient phosphor [6]. Various zinc oxide materials, as a rule, demonstrate two luminescence bands, i.e., a narrow band,

which is located near the absorption edge of the ZnO crystal, so-called the near-band (NBE) emission, and a broad longer wavelength band, the maximum of which is usually in the green spectral range [6] but can be shifted to yellow and even red range. The latter band is called the deep band emission (DBE), or green luminescence (GL). The NBE luminescence with the decay time of about ns has an excitonic nature [7], while the GL with a much longer decay time has a defect nature [6]. UV light-emitters, scintillators, varistors, phosphors, piezoelectric transducers, gas-sensors, etc., have been developed on the base of these materials [3,5,6,8,9]. ZnO is also used in cosmetics, in pharmaceutical, textile and rubber branches of industry [9-11].

ZnO normally crystallizes in the hexagonal (wurtzite) crystal structure with lattice parameters a=3.25 Å and c= 5.21 Å. The Zn^{2+} ions are tetrahedrally coordinated by four O^{2-} ions. The hexagonal prism, positive and negative pedions and the hexagonal pyramid are simple forms characteristic of ZnO crystals [12,13]. The polar planes of pedions have an increased reactivity, which plays an important role in interaction of crystals with doping ions. It was demonstrated that the optical and luminescence characteristics of ZnO largely depend on the choice of the corresponding doping ions, the synthesis conditions and subsequent secondary treatments of the samples [6].

Growth of large ZnO single crystals of high optical quality is time-consuming and a laborious process [6]. The use of ZnO powder with typical particle agglomeration is complicated for many optical applications. The reproducibility of their properties is challenging. The usage of ZnO-based films is limited by optical losses in the substrate material, at the substrate-film interface and within the film. Therefore, the development of nanophase transparent glass-ceramics and optical ceramics based on ZnO crystals doped with transition metal (TM) and rare-earth (RE) ions for optoelectronics is important.

Preparation of transparent glass-ceramics by the melt-quenching technique with subsequent controlled crystallization and fabrication of ceramics by the recrystallization mechanism during hot pressing, respectively, is not only much cheaper and technologically advanced than the growth of single crystals, but also provides high uniformity of properties for relatively large-sized products.

However, there is a difficulty in preparing transparent highly dense polycrystalline ZnO ceramics with anisotropic crystals of hexagonal symmetry. Anisotropic grains in the ceramics cause considerable light scattering at randomly oriented grain boundaries resulting in light losses in the bulk [6]. Therefore, special attention should be paid to the preparation of precursor powders including the search for the optimal size and habitus of particles and the method of doping these powders with impurity ions. Moreover, the relationship between the parameters of hot pressing and the morphology, grain size, texture, transparency and spectral-luminescent characteristics of ceramics should be formulated for the fabrication of ZnO optical ceramics with high transparency and desired properties. Only few research groups succeeded in fabrication of ZnO optical ceramics [6,14-18].

As opposed to rare studies on the ZnO optical ceramic, numerous attempts were made to create ZnO nanostructures (quantum dots and nanocrystals) in glasses of different systems. However, in most of the studies volume crystallization of ZnO was not achieved. For instance, in [19], G. Chen *et al.* observed a broad emission band around 396 nm in initial and heat-treated X-

ray amorphous glass of the SiO_2–B_2O_3–ZnO ternary system where the concentration of ZnO reached 60 mol%. The authors suggested this emission belongs to a ZnO nanophase not detected by XRD method, most probably to a trap-related emission situated at the aggregate – host interface and tried to prove it providing the XRD pattern of a sample crystallized after heating under the extreme conditions. The authors concluded that all the peaks of this material belong to ZnO crystals in different orientations (Fig. 1(b) of the ref. [19]). Meanwhile, the presented XRD pattern [19] demonstrated peaks not of ZnO but of β- and α-willemite. Thus, the ZnO aggregation in the glass was not proven. In [20,21], the authors registered the UV emission in ZnO containing glasses of barium silicate [20,21], barium borate and barium germanate [20] systems and assumed it originated from ZnO aggregation. However, no experimental evidence of ZnO aggregation was provided. In [22], formation of "free ZnO" [22] was suggested in glasses of the SiO_2–ZnO–BaO and the SiO_2–ZnO–BaO–BaF_2 systems based on their photoluminescence spectra. G. Qian *et al.* tried to confirm formation of "free ZnO" by the XRD pattern of the crystallized sample. The authors suggested that the XRD pattern of the crystallized sample 7 (Fig. 4 of ref. [22] presented ZnO while there was a mixture of β- and α-willemite. So, structural evidence of "free ZnO" formation also was not provided. In [23], nanoscale ZnO clusters of amorphous nature were detected in oxynitride zinc phosphate glass using TEM.

Not volume but surface crystallization of ZnO was achieved in studies [24-28] for materials based on the borate glass of the CaO–B_2O_3–ZnO–Al_2O_3–K_2O–SiO_2 system and in [29,30] for glasses of similar compositions. In [31], surface crystallization of willemite and zinc oxide was demonstrated. In [32], surface crystallization of ZnO was observed in zinc-boro-oxy-fluoride glass. Thus, we came to conclusion that in all mentioned above systems volume crystallization of zinc oxide was not achieved.

There are several studies devoted to ZnO nanoparticles with size of about 3-6 nm obtained in SiO_2 matrix via a sol-gel route [33-36]. Partially crystallized samples with ZnO crystals were obtained in supercooled melts consisting of 70-80 mol% ZnO, up to 20 mol% B_2O_3 and SiO_2 by Dimitriev et al. [37]. ZnO nanocrystals formed on the surface of glass of the ZnO–B_2O_3–SiO_2–Sm_2O_3 system by laser pattering were reported in [38]. In [39], the CO_2 laser-treated glasses of the CaO–B_2O_3–ZnO–Al_2O_3–K_2O system demonstrated surface crystallization of Ag and ZnO nanocrystals.

Transparent glass-ceramics based on volume crystallized zincite (ZnO) nanocrystals were first obtained by L. Pinckney [40] in the K_2O- ZnO-Al_2O_3-SiO_2 system. The compositions were designed as the ZnO component in a stoichiometric to subsiliceous leucite ($K_2O{\cdot}Al_2O_3{\cdot}4SiO_2$) residual glass. L. Pinckney revealed that gallium can be substituted in part for aluminum and sodium in part for potassium without deteriorating properties and that contents of SiO_2 higher than 50 wt% or Na_2O higher than 12 wt% tend to promote the crystallization of willemite (Zn_2SiO_4) rather than ZnO [40]. L. Pinckney suggested that in the process of formation of glass-ceramics, phase separation was induced between alkali aluminosilicate and lower silica, high - zinc glasses. The low - silica phase extremely rich in ZnO, yields zincite from 5 to 20 nm in size upon heat-treatment to 750 °C [41]. In [40], the main features of the ZnO crystallization were revealed and doping of these glass-ceramics with TM and RE ions was discussed.

Up to now, in studies on volume crystallization of ZnO and spectroscopic properties of ZnO-containing transparent glass-ceramics, the authors [42-55] use the ideas and glass compositions suggested by L. Pinckney in ref. [40]. Even space-selective precipitation of ZnO crystals by using high repetition rate femtosecond laser irradiation was reported in [56] for the glass with the composition of $45SiO_2$-$15Al_2O_3$-25ZnO-$15K_2O$ (mol%), which belongs to the system developed by L. Pinckney [40].

We have found only one excellent paper [57] wherein glass-ceramics containing ZnO nanosized crystals were obtained in a different system. Though it was formally the same potassium zinc aluminosilicate system, the difference with compositions presented in [40] was in the substitution of zinc oxide with zinc fluoride, which resulted in glass of the oxifluoride composition. It produced a significant difference in the phase composition of glass-ceramics: a mixture of ZnO and β-Zn_2SiO_4 precipitated simultaneously at the initial stage of heat-treatment, whereas sole crystallization of ZnO occurred when heat-treatments were performed at a higher temperature. This sequence of phase transformations is opposite to that presented in [40] and probably originates from the different mechanism of phase separation in glasses of the oxifluoride potassium zinc aluminosilicate system as compared with the oxide one.

Transparent glass-ceramics based on semiconducting ZnO crystals are self-nucleating materials due to liquid-liquid phase separation [40], which makes the sequence of phase transformations of initial glasses and properties of glass-ceramics extremely dependent on the preparation conditions (batch weight, crucible material, glass melting temperature, cooling rate, heat-treatment schedule) and purity of the raw materials. Optical properties of transparent glass-ceramics based on ZnO crystals are largely determined by the defect chemistry of the ZnO crystals that have relatively open structure and plenty of sites to accommodate intrinsic defects and extrinsic dopants. That is why optical properties of glass-ceramics depend on the preparation conditions and purity of the raw materials. We would just like to state that in ref. [40] the batch weight was to yield about 1000 g of glass, glasses were melted in platinum crucibles at 1600 °C for 6 h, cast into patties about 1 cm thick, annealed at 575°C for 1 h and crystallized at temperatures of 700–800°C for 1–2 h. Later on, other researchers used different preparation techniques to produce glass-ceramics of similar compositions. In ref. [45] for a similar glass composition, quite a different preparation technique was used: the batch weight was 20 g, glasses were melted in alumina crucibles at 1500 °C for 2 h, subsequently quenched on a steel plate and crystallized at temperature of 750 °C for 3, 5, 10, 30, 60 and 120 min. In [53], the batch weight was 100 g, glasses were melted in alumina crucibles at 1580 °C for 2 h, subsequently quenched onto the preheated steel plate, annealed in a muffle furnace at 500 °C and crystallized at temperature of 730 °C for 0, 5, 8, 15, 30, 60 min. Thus, it is extremely important to pay a special attention to the preparation conditions while comparing the properties of ZnO-based glass-ceramics of similar compositions prepared by different research groups.

The present work aims at comparing the structure of multiphase transparent glass-ceramics based on ZnO nanocrystals prepared from glasses of the K_2O- ZnO-Al_2O_3-SiO_2 system by controlled crystallization and of ZnO optical ceramics produced by recrystallization high-temperature pressing and doped with RE and TM ions. The section devoted to fabrication, phase

transformations and structure of ZnO-based glass-ceramics is composed in such a manner as to illustrate the ideas presented in ref. [40] by our original results.
This paper is a tribute to Linda Pinckney.

2. Experimental

2.1. Preparation of glasses and glass-ceramics

We used initial glasses of two different compositions of the K_2O - ZnO - Al_2O_3 - SiO_2 system. The first composition, 12 K_2O, 28 ZnO, 12 Al_2O_3, 48 SiO_2 (mol%), is similar to the composition Z4 listed in *Table 1, Compositions of transparent ZnO glass-ceramics*, of the ref. [40]. The second composition is 14 K_2O, 32 ZnO, 14 Al_2O_3, 40 SiO_2 (mol%). Batches of the first composition (Zn1) 200 g in weight were melted in a platinum crucible. Batches of the second composition (Zn2) 400 g in weight were melted in crucibles made of quartz ceramics.

The glass batches were prepared of reagent grade K_2CO_3, ZnO, Al_2O_3 and SiO_2. TM oxides (Co_3O_4, Cr_2O_3, Ni_2O_3, CuO), and RE oxides (Tm_2O_3, Er_2O_3, Yb_2O_3, Eu_2O_3, (Er_2O_3+Yb_2O_3), (Eu_2O_3+ Yb_2O_3) were added above 100 mol% of the base components. All the components were carefully mixed before being placed into the crucible. Glasses were melted in a laboratory electric furnace at 1590 °C for 3 h with stirring, poured onto a cold metal plate and annealed at 500 or 550 °C. All glass-ceramics, undoped and doped with TM and RE oxides in concentration of 0.01-2.0 mol%, were prepared by secondary heat treatments of initial glasses in the temperature range from 680 to 1300 °C for 2 to 100 hours. The examples of transparent ZnO glass-ceramics, undoped and doped with TM and RE ions, are shown in Fig. 1.

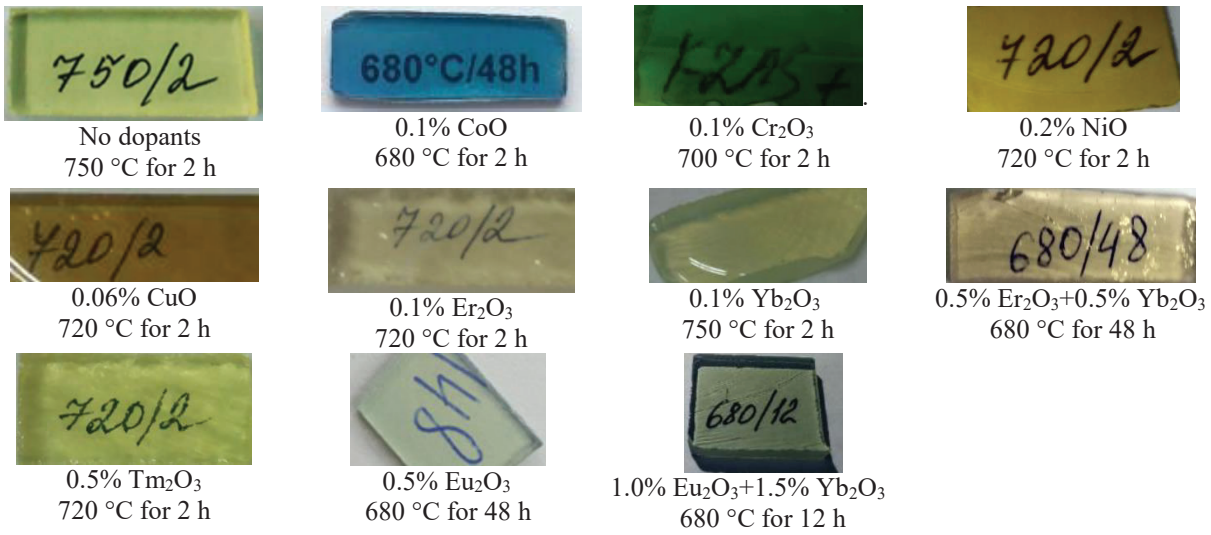

Figure 1. Photographs of transparent ZnO glass-ceramics, undoped and doped with TM and RE oxides.

2.2. Preparation of ceramics

The undoped, Co-, Er-, Yb-doped and Er, Yb co-doped ZnO optical ceramics with the cobalt and RE ions concentration of 0.1-5.0 wt% were fabricated from commercial reagent grade ZnO (purity: 3N, Zinsa, Peru), Co_3O_4 and RE oxides of the same purity. The weighted portions of reagents were thoroughly mixed. The ceramics were prepared by uniaxial hot pressing

(HPing) in vacuum at 1150 - 1220 °C. Both sides of the as-sintered ceramic disks were mirror polished using diamond slurry. After polishing, the disks had a diameter of 25 mm and a thickness of about 0.5 mm. The undoped ZnO ceramic is of yellow-green color. With Er^{3+} and Yb^{3+} doping, the color changed to rose and grey, respectively. The cobalt-doped ceramics are emerald-green colored. The color intensity increases with increasing the cobalt concentration in such a manner that the sample doped with 5%CoO was black. The examples of transparent undoped, Er- ,Yb, (Er_Yb) and Co-doped ZnO ceramics are shown in Fig. 2.

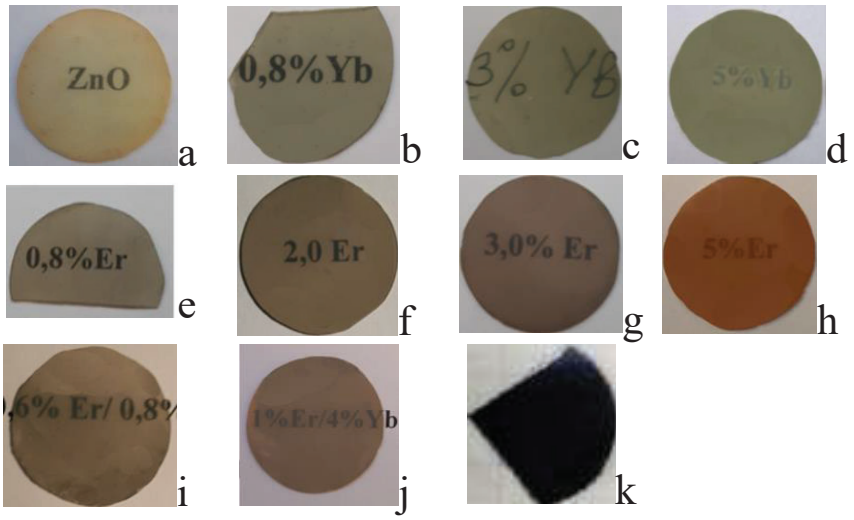

Figure 2. Photographs of (a) undoped, (b-d) ZnO:(0.8-5.0)Yb, (e-h) ZnO:(0.8-5.0)Er, (i) ZnO:(0.6Er/0.8Yb), (j) ZnO:(1Er/4Yb), (k) ZnO:5Co transparent ceramics. The RE and TM ions doping level is in wt%.

2.3. Characterization methods

2.3.1. Differential scanning calorimetry (DSC)

Glasses were characterized by differential scanning calorimetry (DSC) measurements performed on a simultaneous thermal analyzer NETZSCH STA 449 F3 Jupiter. The glass transition and crystallization temperatures were determined from about 15 mg bulk samples, using platinum crucibles and argon as a purging gas at the temperature range between room temperature and 1250 °C. The heating rate was 10 °C/min.

2.3.2. X-ray diffraction (XRD) analysis

XRD patterns of finely powdered initial glasses and glass-ceramics were measured using a Shimadzu XRD-6000 diffractometer with Cu Kα radiation and a Ni filter (λ=1.54 Å). Taking into account that the phase assemblage on the surface and in the volume of glass-ceramics can differ, XRD patterns, if necessary, were taken not only from the volume of the sample, but also from its surface. In this case, the volume and the surface of the sample were carefully separated. The XRD patterns were collected in a fixed time scan, sampling pitch: 0.02◦, preset time: 6 s. We performed Rietveld refinement of the structure, phase compositions, volume fraction and sizes of nanocrystals using the Maud program [58]. Pure cubic Y_2O_3 powder standard sample was used to correct the data for instrumental broadening. For modeling the residual glass [59], we used the leucite, $KAlSi_2O_6$. The mean crystal size and volume fraction of ZnO were

determined. The error in the estimation of the mean crystal size is about ±2 nm for D_{XRD} of about 20–30 nm [60]. The error in the estimation of the volume fraction of ZnO depends on the volume fraction and was estimated according to Ref. [59]. Parts of XRD patterns of the glass-ceramics after heat-treatments at 1200 and 1300 °C were recorded in a scanning mode (2θ=27.6–29.8°) with a sampling pitch of 0.04° and a 100 s preset time.

The XRD patterns of ceramic disks were measured using the same Shimadzu XRD-6000 diffractometer with a Ni-filtered Cu K_α radiation. The samples were scanned according to a following mode: fixed time scan, scan speed 2.0 degree/min, sampling pitch: 0.02°, preset time: 3.0 s. To check whether crystals of rare-earth oxides were formed during sintering, additional XRD patterns were recorded in a special mode (fixed time scan, sampling pitch: 0.01°, preset time: 100 s) in an angular range of 2θ = 29.0-30.3°, where the main diffraction peaks of cubic Yb_2O_3 and Er_2O_3 are located. With the aim to find the cobalt-containing crystalline phase, additional XRD patterns were also recorded in another special mode (fixed time scan, sampling pitch: 0.03°, preset time: 60 s) in the angular ranges of 2θ = 42.0-42.99° and 2θ = 61.0-61.99°, where the diffraction peaks of cubic CoO with Miller's indices *(hkl)* (200) and (220), respectively, are located. The Rietveld refinement was performed using the Maud software [57].

For evaluating the preferred orientation of ZnO samples, the texture coefficient $T_c(hkl)$ was used. It was calculated by the equation (1):

$$T_c(hkl) = \frac{I(hkl)/I_0(hkl)}{(1/N)\left[\sum_N I(hkl)/I_0(hkl)\right]}, \quad (1)$$

where (*hkl*) is the crystalline plane, I is the measured XRD intensity, I_0 is the standard intensity of randomly oriented crystals according to a reference XRD card and N is the number of diffraction peaks [61]. From Eq. (1) it follows that T_c is close to unity for randomly oriented crystals, and it is greater than 1 when a certain (*hkl*) plane is preferentially oriented.

2.3.3. Small angle X-ray scattering

Plane-parallel polished samples with thickness of 0.2 mm were studied by small angle X-ray scattering (SAXS) method. The SAXS intensity I(φ) was measured with a home-made instrument in the range of scattering angles φ from 6 to 450 arc min which corresponds to scattering vector range (Q) from $8\cdot10^{-3}$ Å^{-1} to 0.5 Å^{-1} where $Q = (4\pi/\lambda)\sin(\varphi/2)$, λ is the X-ray wavelength and φ is a scattering angle. CuKα radiation (λ =1.54 Å) was used with an "infinitely" high primary beam ("infinitely" high slit).

SAXS curves of phase-separated glasses and glass-ceramics often exhibit maximum. It appears due to the regularity in a distribution of scattering regions in the glass volume. The value of Q corresponding to the maximum on the I(Q) curve (Q_0) and the distance between centers of regularly distributed particle (L) are related as

$$L \cong (3.3 \div 3.5)10^3 Q_0^{-1} \quad (2)$$

where L (in Å) is a distance between centers of regularly distributed particle [62]. The position of the maximum Q_m on the Q dependence of Q·I(Q) corresponds to the inverse radius of the scattering regions. For the monodisperse system of spherical particles with radius R, in condition of validity of Guineir equation [63]

$$R = \sqrt{\frac{5}{2}} Q_m^{-1} \qquad (3).$$

2.3.4. Electron microscopy

The structure of the initial glass and glass-ceramics was studied by the transmission electron microscopy (TEM) with the JEOL TEM-1011 microscope (100 kV acceleration voltage, 0.4 nm point resolution). Fine powdered materials were dispersed in ethanol, and a drop containing a small amount of material in suspension was deposited onto a carbon-coated copper grid.

The morphology of ceramics was characterized by scanning electron microscopy (SEM) using TESCAN LYRAS and Carl Zeiss MERLIN microscopes. For the study by the Carl Zeiss MERLIN microscope, the surface of ceramics was preliminary etched in a mixture of hydrochloric and hydrofluoric acids. The same MERLIN microscope equipped with an Inca Energy X-Max analyzer was employed for energy dispersive X-ray (EDX) based element mapping.

2.3.5. Raman spectroscopy

The Raman spectra were measured with a Renishaw inVia confocal Raman microscope equipped with the multichannel detector cooled down to −70 °C using a Leica x50 objective (N.A. = 0.75). The accumulation time was 10 s and the number of accumulations was 30. The spatial resolution was about 2 cm^{-1}. The Raman spectra of glasses and glass-ceramics were recorded using the excitation wavelength λ_{exc} of 488 nm (Ar^+ laser line). An edge filter was used. The Raman spectra of ceramics were measured using the excitation wavelength λ_{exc} of 514 nm (Ar^+ laser line).

2.3.6. Optical spectroscopy

The optical absorption spectra of initial glasses, glass-ceramics and ceramics were measured in the spectral range from 300 to 3300 nm with a Shimadzu UV 3600 spectrophotometer with a spectral resolution of 1 nm (0.2 nm for the range of absorption bands of RE ions). The plane-parallels polished samples were used.

It should be taken into account that glass-ceramics are inhomogeneous materials (they contain crystals in a glass matrix) and scatter light. Thus, the measurement of optical density of a glass-ceramic sample is accompanied by falling the scattered light into a detector of the spectrophotometer that leads to an error in optical density measurement. The error depends on scattering characteristics and the acceptance angle of the spectrophotometer. Previously, we studied the problem of measuring optical density of nanostructured glass-ceramics samples by the spectrophotometer Shimadzu UV 3600 [64] and concluded that the error is negligible if the internal optical density of the sample caused by scattering, D_s, satisfies the condition

$$D_s \lesssim 2. \qquad (4)$$

We checked the fulfilment of this condition in all our measurements of optical density of glass-ceramic samples.

3. Results

3.1. Glasses and glass-ceramics

3.1.1. SAXS and XRD analysis of glasses and glass-ceramics

SAXS is a powerful tool to study early stages of formation of inhomogeneity regions in glasses inclined to phase separation [63]. The potentiality of SAXS in the study of glass-ceramic structure was described in detail (for example, see [65] and references therein). The structure of the initial glass Zn1 doped by 0.05% CoO and ZnO-based glass-ceramics prepared from this glass by heat-treatments at 680 °C for 24 h and at 720 °C for 2 h was studied by SAXS. Fig. 3(a) shows SAXS intensity I as a function of the magnitude of scattering vector Q.

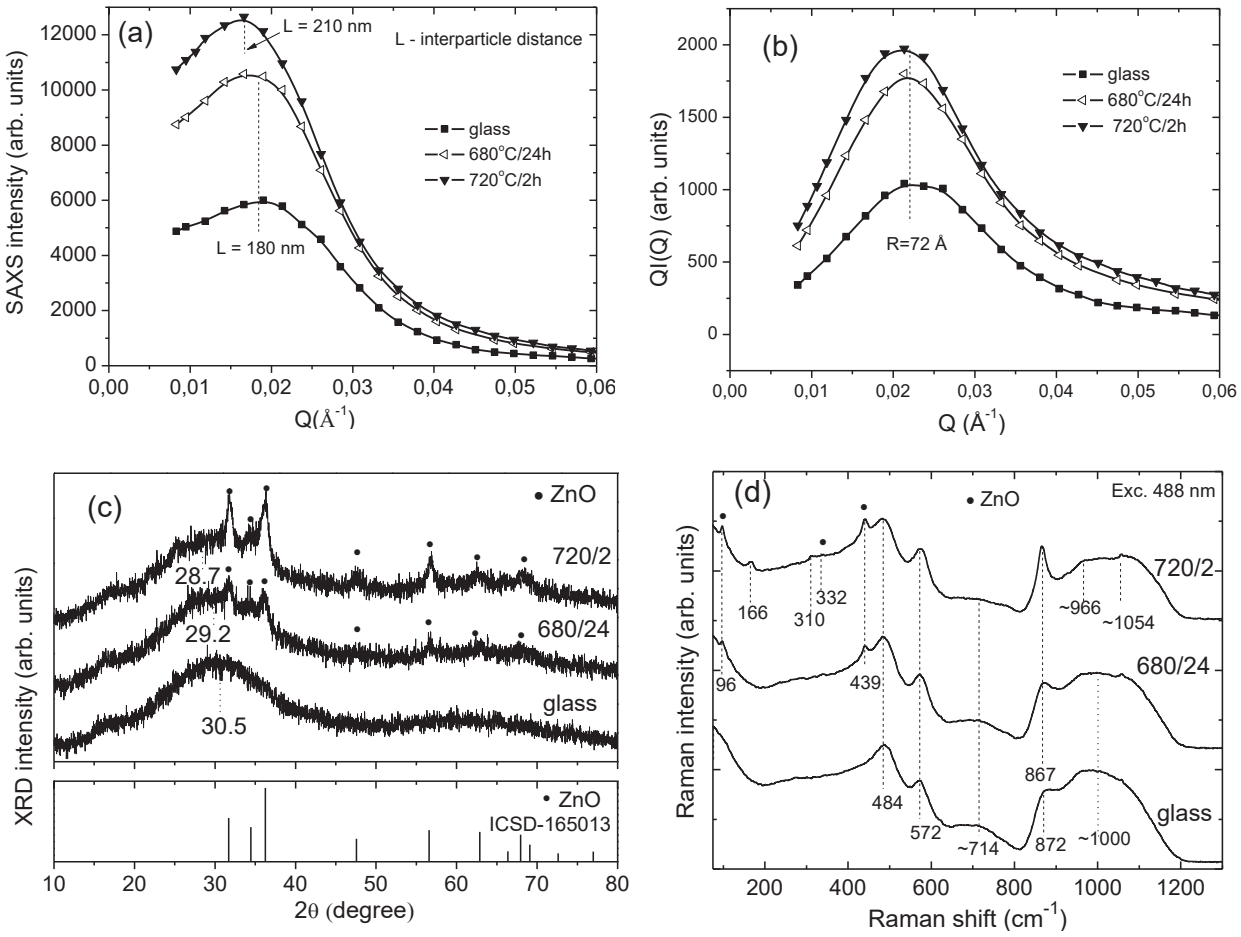

Figure 3. SAXS curves and XRD patterns for the initial glass Zn1 doped with 0.05% CoO and glass-ceramics: (a) dependences of the SAXS intensity on Q; (b) dependences of Q·I(Q) on Q; (c) corresponding XRD patterns and the standard pattern of ZnO; (d) Raman spectra. The dashed lines mark the positions of the maxima on the curves. The heat-treatment schedules, °C / duration, hours, are shown in figures.

According to SAXS, Fig. 3(a,b), and XRD findings, Fig. 3(c), the initial glass is inhomogeneous and X-ray amorphous. After heat-treatments, the SAXS intensity increases. The angular dependences of the SAXS intensity by the initial glass and the glasses heat-treated at 680 and 720 °C demonstrate pronounced maxima, see Fig. 3(a). After the heat-treatment of the initial glass at 680 °C for 24 h, the position of the maximum remains practically unchanged. According

to Eq. (2), from the position of the maximum, it follows that the mean interparticle distance is about 180 Å both in the initial glass and in glass-ceramics prepared by the heat-treatment at 680 °C for 24 h. The presence of a maximum on the angular dependence of the SAXS intensity by the initial glass can be considered as an evidence of spinodal phase decomposition that occurs during cooling of the glass melt [65]. The invariability of the position of this maximum after the heat-treatment at 680 °C for 24 h means that the space distribution of inhomogeneous regions formed in the glass during its casting and annealing is not changed during this heat-treatment. Heat-treatment at 720 °C for 2 h leads to a shift of the maximum on the SAXS curve to smaller angles, and the interparticle distance increases to 210 Å.

Fig. 3(b) shows the dependences of Q·I(Q) versus Q for the initial glass and glass-ceramics. The position of the maximum on the Q·I(Q) curve by the glass remains near constant after its heat-treatment at 680 °C for 24 h, i.e., the dimensions of the scattering regions formed in the initial glass remain unchanged and equal to ~70 Å. Consequently, the increase in the SAXS intensity should be related to crystallization of ZnO within these inhomogeneous regions occurring during heat-treatment, see Fig. 3(c). When the glass was heat-treated at 680 °C for 24 h, the number of inhomogeneous regions did not change. The Ostwald ripening was not observed. Thus, the liquid phase separation was actually completed during cooling of the melt. Crystallization occurs within the liquid phase-separated regions. The spinodal character of decomposition at melt quenching and annealing does not exclude the formation of a droplet structure at later stages of phase transformation during subsequent heat-treatments [66]. Crystallization occurs independently in each droplet.

These findings confirm the statement of L. Pinckney that "*The ZnO-based glass-ceramics are self-nucleating due to liquid-liquid phase separation and require no added nucleating agents" [40]*.

3.1.2. The Raman spectroscopy study of glasses and glass-ceramics

Fig. 3(d) shows Raman spectra of the initial and heat-treated glass Zn1 doped with 0.05% CoO. Note that their XRD patterns are listed in Fig. 3(c). Similar Raman spectra were presented by Du et al. for ZnO crystals prepared by space-selective precipitation in glass using femtosecond laser irradiation [56]. The Raman spectrum of the initial glass consists of the main band with peaks at 484, 572 and 714 cm^{-1} and the high-frequency envelope with the maxima at ~872, and ~1000 cm^{-1}. According to [67], the band near 484 cm^{-1} indicates Si-O-Al linkages, the shoulder resolved at 572 cm^{-1} implies the presence of Al-O-Al bridges [67,68], while the high-frequency envelope is due to the antisymmetric-stretching modes of O atoms and network-forming cations in the three-dimensional aluminosilicate framework [67,69]. After heat-treatment of the initial glass at 680 °C for 24 h, the new peaks appear at 96 and 438 cm^{-1} that are assigned to the E_2^{low} and E_2^{high} modes of hexagonal ZnO crystals [70,71]. The shape of the high-frequency envelope in the spectrum of the sample is changed. Instead of the unresolved band at ~872 cm^{-1}, the peak at 867 cm^{-1} appears. The higher frequency band broadens, see Fig. 3(d). After heat-treatment at 720 °C for 2 h, in addition to the peaks at 96 and 438 cm^{-1} the tiny peak appears at 332 cm^{-1}. This peak is assigned to E_2^{low} and E_2^{high} modes difference in Raman spectrum of ZnO crystals [70]. The appearance of small peaks at 166 and 310 cm^{-1} as well as

narrowing and intensification of the peak at 867 cm^{-1} manifests the continuation of structure ordering within the silicate regions enriched in zinc. With further increasing the heat-treatment temperature, this ordering will result in additional crystallization of β-willemite, β-Zn_2SiO_4 [72]. The high frequency envelope in the Raman spectrum becomes broader due to appearance of the maximum at ~1054 cm^{-1}. This change can be explained by the increased connectivity of the aluminosilicate network caused by the ZnO crystallization [71,72]. We did not find the spectrum of glass with leucite composition in the literature, however, there is the spectrum of amorphous leucite obtained at high pressure [73] and its high-frequency envelope is consistent with those of the glass-ceramics obtained presented in Fig. 3(d). The Raman spectra of the SiO_2–$KAlSi_3O_8$ glass series [67] also demonstrate similar features.

An analysis of the position of the amorphous halo in the XRD patterns of the samples under study confirms these findings, see Fig. 3(c). The maximum of the diffuse X-ray scattering by the initial glass is at $2\theta \approx 30.5°$. All components of the initial glass contribute to this scattering. During heat-treatments at 680 °C for 24 h and 720 °C for 2 h, ZnO crystals are formed in the glass. Crystallization of ZnO is accompanied by a change in the composition of the residual glass phase, as evidenced by the shift of the diffuse maximum to $2\theta \approx 29.2°$ and then to 28.7°. The main contribution to this scattering is made by potassium aluminosilicates. Note that the strongest diffraction peak in the XRD pattern of kalsilite is located at $2\theta \approx 28.6°$; other potassium feldspars also have strong lines in this angular range.

These findings confirm the statement of L. Pinckney that "*The compositions can be approximated as the ZnO component in a stoichiometric to subsiliceous leucite host glass… The microstructure of the transparent glass-ceramic comprises 5–20 nm crystals of ZnO dispersed uniformly throughout a continuous aluminosilicate glass [40]*.

3.1.3. The DSC and XRD studies of glasses and glass-ceramics

Fig. 4(a) shows a typical DSC curve by the example of the Z1 initial glass doped with 0.05% CoO. For this glass, T_g is at ~660 °C, the ZnO onset crystallization temperature is ~760 °C. The peak connected with crystallization of β-willemite (β-Zn_2SiO_4) appears at higher temperature of about 800 °C but its onset crystallization temperature is difficult to determine because this peak superimposes on the peak of ZnO. The onset crystallization temperature of α-willemite (α-Zn_2SiO_4) is ~989 °C and that of leucite ($K_2O{\cdot}Al_2O_3{\cdot}4SiO_2$) is ~1120 °C.

This crystallization sequence is demonstrated in Fig. 4(b) by the example of the same Z1 glass doped with 0.05% CoO. No diffraction peaks are found in the XRD pattern of the initial glass indicating that it is X-ray amorphous. The first phase to crystallize is ZnO; it appears during heat-treatments at temperature of 680 - 720 °C. The mean ZnO crystal sizes determined using the Scherrer equation are about 10 - 11 nm [71]. Heat-treatments in the temperature range of 750 – 900 °C resulted in crystallization of a mixture of ZnO and β-Zn_2SiO_4 nanocrystals. Their mean sizes determined with the Scherrer equation are about 10 - 12 nm and 11-14 nm, respectively, depending on the heat-treatment temperature [72]. α-willemite crystallizes at 950 °C at the expense of ZnO and β-Zn_2SiO_4. During heat-treatment at 1000 °C, leucite ($K_2O{\cdot}Al_2O_3{\cdot}4SiO_2$) additionally crystallizes from the surface, while kalsilite ($K_2O{\cdot}Al_2O_3{\cdot}2SiO_2$) crystallizes in the volume of glass-ceramic, see Fig. 4(c). At elevated temperatures, the main

crystalline phases are α-willemite and leucite while the traces of kalsilite are still observed, see Fig. 4(b).

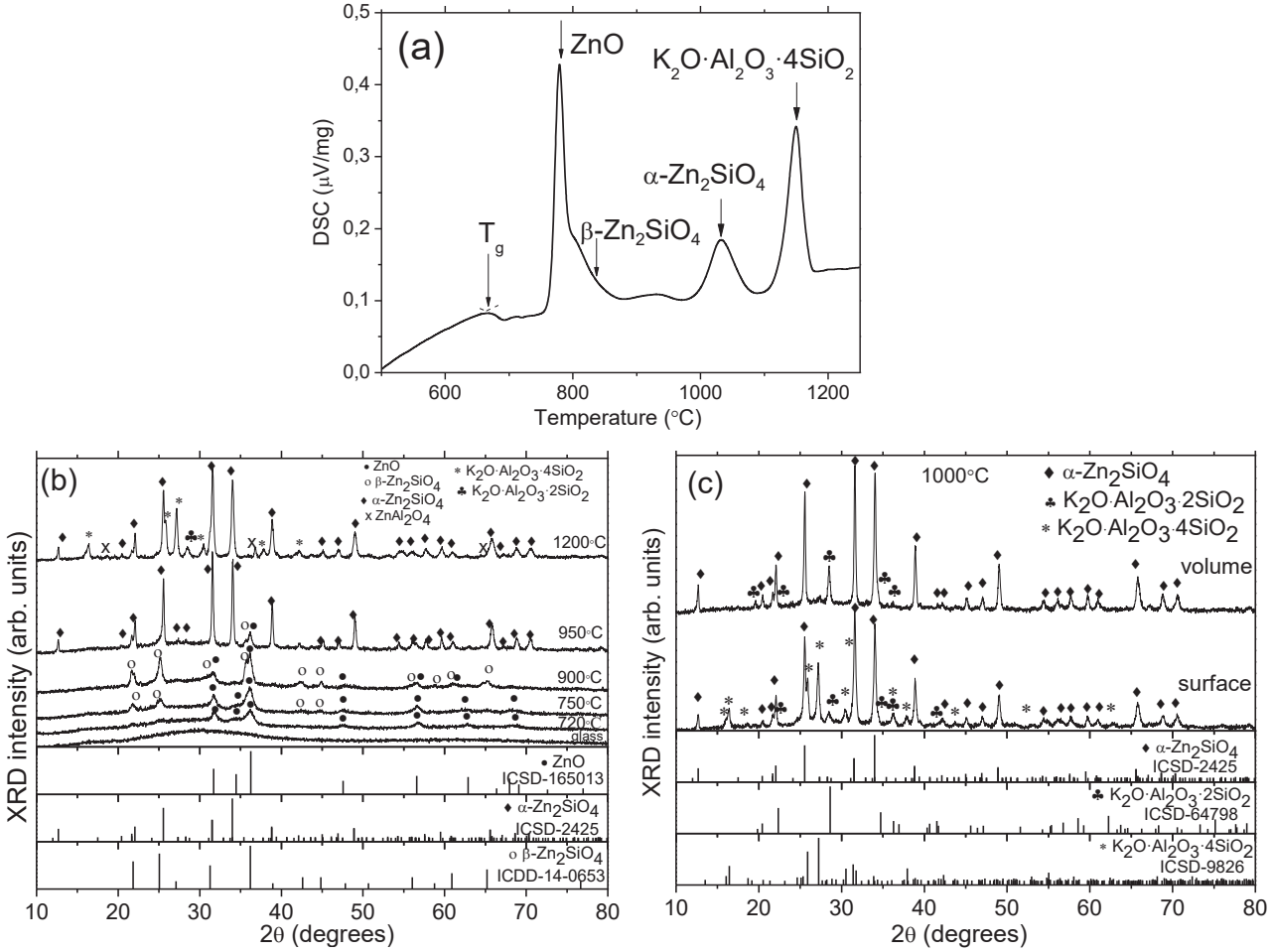

Figure 4. DSC curve (a) and XRD patterns (b,c) of the initial and heat-treated glass Zn1 doped with 0.05% CoO. (b) Heat-treatment temperatures are listed in the figure. (c) The XRD patterns of the surface and the volume of glass-ceramic prepared by the heat-treatment at 1000 °C. Heat-treatment time is 2 h. Standard XRD patterns of ZnO, β-Zn_2SiO_4, α-Zn_2SiO_4, $K_2O·Al_2O_3·4SiO_2$ and $K_2O·Al_2O_3·2SiO_2$ are presented.

These findings confirm the statement of L. Pinckney that "*Zinc oxide is the first phase to crystallise as temperature increases, followed by the crystallisation and growth of willemite at the expense of ZnO and eventually to the surface crystallization of leucite ($KAlSi_2O_6$) at the expense of the residual glass" [40].*

3.1.4. Study of glass-ceramics doped with TM ions (optical spectroscopy and XRD analysis)

3.1.4.1. Cobalt-doped glass-ceramics

Fig. 5(a,b) demonstrates absorption spectra and corresponding XRD patterns of the initial and heat-treated glass Zn1 doped with 0.1 mol% CoO. The spectrum of the initial glass, see Fig. 5(a), contains two broad absorption bands, one with maxima at 525, 590, and 640 nm, and the

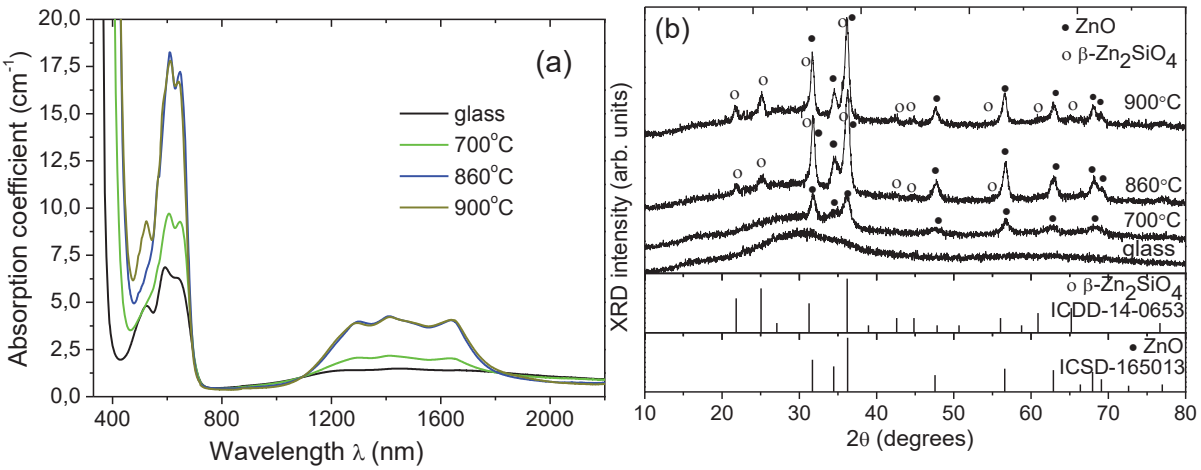

Figure 5. Absorption spectra (a) and corresponding XRD patterns (b) of the initial and heat-treated glass Zn1 doped with 0.1% CoO. Standard XRD patterns of ZnO and β-Zn_2SiO_4 are presented. Heat-treatment temperatures are listed in the figure. Heat-treatment time is 2 h.

other in the range of 1100–1700 nm. It is characteristic of Co^{2+} ions in a mixture of coordination sites: in octahedral, in distorted tetrahedral coordination, and possibly in five-fold coordinated sites. This type of spectrum is typical for Co^{2+} ions in aluminosilicate glasses [71]. A change in the absorption spectrum of the sample is observed after its heat-treatment at 700 °C for 2 h. There is a reduction of absorption at ~525 nm, appearance of a shoulder at ~565 nm and of absorption bands at 607 and 643 nm. The broad band in the 1.2–1.7 μm range becomes narrower and demonstrates peaks located at ~1.29, 1.42, 1.49, and 1.64 μm. This change is caused by crystallization of ZnO, Fig. 5(b), and entering the tetrahedral sites in these nanocrystals by the Co^{2+} ions. The observed absorption bands match those for Co^{2+}:ZnO [74-76] and they are attributed to d-d transitions of Co^{2+} ions with $3d^7$ high-spin configuration in a tetrahedral ligand field formed by neighboring oxygen ions in ZnO nanocrystals [71,72]. The absorption peaks in the visible range are assigned to $^4A_2(F) \rightarrow {}^2E(G)$, $^4A_2(F) \rightarrow {}^4T_1(P)$, and $^4A_2(F) \rightarrow {}^2A_1(G)$ transitions. The absorption band in the infrared is associated with the electronic transitions from the $^4A_2(F)$ ground-state to the $^4T_1(F)$ excited multiplet. Intensities of these peaks constantly increase with heat-treatments at temperatures up to 860 °C and correspond to increasing the volume fraction of ZnO nanocrystals, Fig. 5(b). Appearance of the peak at 523 nm in the spectrum of the glass-ceramic prepared by the heat-treatment at 900 °C is connected with Co^{2+} absorption both in octahedral and in distorted tetrahedral sites in β-willemite crystals [72]. The diffraction peaks of β-willemite crystals are clearly seen in Fig. 5(b).

3.1.4.2. Nickel-doped glass-ceramics

Fig. 6(a-c) presents absorption spectra and corresponding XRD patterns of the initial and heat-treated glass Zn1 doped with 0.2 mol% NiO. The absorption spectrum of the initial glass presents three broad asymmetric absorption bands centered at about 439, 870 and 1830 nm. It is typical for Ni-doped aluminosilicate glasses and can be assigned to absorption of trigonal bipyramid fivefold Ni2+[V] and tetrahedral fourfold species [77] with the predominance of $Ni^{2+[V]}$ species. A change in the absorption spectrum of the sample is observed after its heat-

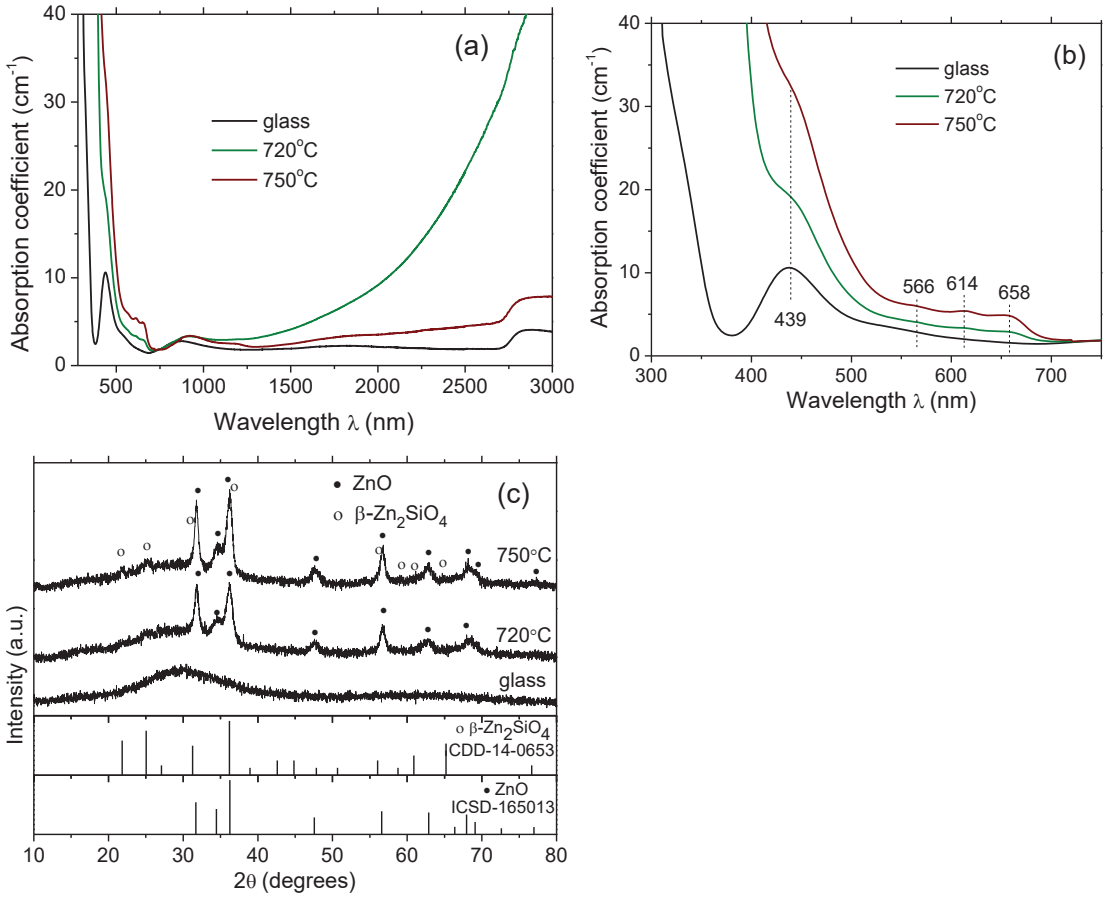

Figure 6. Absorption spectra of the initial and heat-treated glass Zn1 doped with 0.2 mol% NiO (a,b) in the spectral range of 300 – 3000 nm (a), in the spectral range of 300 – 750 nm (b); corresponding XRD patterns and standard XRD patterns of ZnO and β-Zn_2SiO_4 (c). Heat-treatment temperatures are listed in the figure. Heat-treatment time is 2 h.

treatment at 720 °C for 2 h. The absorption edge is shifted to longer wavelengths in such a manner that the absorption band with the maximum at 439 nm becomes partly concealed, new bands appear at 566, 614, 658, 742, ~920 nm, and ~1199, the raise of absorption at wavelengths longer than 1000 nm is revealed. The maximum of this IR absorption is not detected up to 3300 nm, which is the measurement limit of the spectrophotometer. These spectral changes are connected with crystallization of ZnO, see Fig. 6(c), and partition of Ni^{2+} ions in these crystals [40]. Indeed, Pappalardo *et al*. [78] suggested that in ZnO, the Ni^{2+} impurity ions are present in sites possessing tetrahedral symmetry with a slight axial deformation. The crystal field parameter Dq_{tet}≈380 cm^{-1}. The absorption peaks of Ni^{2+} ions in ZnO are located at 576, 616, 656, 742, and 1192 nm [78]. These peak positions are very similar to those in spectrum of the glass-ceramic sample, see Fig. 6(b). The raise of absorption in the IR is related to the presence of free carriers in semiconductor ZnO nanocrystals [79]. Thus, the spectrum is a superposition of spectral features of Ni^{2+} ions distributed between the ZnO crystals and the residual glass and the spectral features of ZnO nanocrystals.

It confirms the statement that *"The absorption peaks coincide with those reported by Pappalardo et al. for tetrahedrally coordinated Ni^{2+} in ZnO, indicating that at least some of the Ni^{2+} ions have partitioned into the ZnO crystals" [40]*. We also confirm the statement that all

ZnO-based glass-ceramics doped with TM ions *exhibit a significant colour change upon crystallisation consistent with a change in crystal field environment of the dopant ions, although part of the color change can be attributed to the crystallisation of ZnO itself* [40].

An increase of the heat-treatment temperature by 30 °C causes a significant spectral change, see Fig. 6(a,b). The absorption edge is shifted to even longer wavelengths, intensity of absoption bands with maxima at 566, 614 and 658 nm increases, intensity of the peak with the maximum at ~920 nm remains near constant, and the peak appears at 1185 nm, see Fig. 6(a,b). IR absorption caused by the presence of free carriers in ZnO pronouncedly decreases. We assign these spectral changes to some increase in the ZnO crystallinity fraction and, to the larger extent, to crystallization of β-willemite, see Fig. 6(c). In literature, information about the reflectance spectrum of Ni^{2+}: Zn_2SiO_4, α-willemite, is evaluable [80]. The spectrum exhibits a wide, intense band in the range of 480-760 nm with absorption maxima at 540, 584, and 633 nm, which corresponds to the $^3T_1(F) \rightarrow {}^3T_1(P)$ d-d transition in the tetrahedral environment. We cannot exclude the presence of these peaks in broad absorption bands of glass-ceramic prepared by heat-treatment at 750 °C. It should be taken into account that in β-willemite Ni^{2+} ions can enter both octahedral and in distorted tetrahedral sites crystals. We can find the attributes of $^{[VI]}Ni^{2+}$ in the spectrum of glass-ceramics. According to R. Pappalardo *et al.* [78], the crystal field parameter of Ni^{2+} ion in octahedral site symmetry in MgO crystals $Dq_{oct} \approx 860$ cm^{-1}. Previously, we built the Tanabe-Sugano diagram for $^{[VI]}Ni^{2+}$ ion in the assumption that Dq= 860 cm^{-1} and B=890 cm^{-1} [81]. The following positions of the maxima of absorption band of Ni^{2+} ions were predicted: less than 400 cm^{-1}, 690, 790, and 1160 nm. Thus, the spectrum glass-ceramic sample containing a mixture of ZnO and β-willemite can be assigned to $^{[IV]}Ni^{2+}$ species in ZnO and β-willemite crystals, to $^{[VI]}Ni^{2+}$ species in β-willemite crystals, and to $^{[V]}Ni^2$ species in the residual glass. A decrease of the IR absorption could be related to a beginning of β-willemite crystallization.

3.1.4.3. Chromium-doped glass-ceramics

The absorption spectrum of the Zn1 glass doped with 0.1 mol% Cr_2O_3 contains two broad absorption bands with maxima at 427 and 630 nm, see Fig. 7(a,b). This spectrum is typical for Cr^{3+} ions in d^3 configuration in octahedral sites in silicate and aluminosilicate glasses and corresponds to the interconfigurational transitions from the $^4A_2$ ground state to the $^4T_1$ and $^4T_2$ excited states, respectively [82]. There is also the inflection at 703 nm which corresponds to spin and parity forbidden transitions $^4A_2 \rightarrow (^4T_1, {}^2E)$. The ligand field strength Dq is ~1590 cm^{-1}, the Racah parameter B is ~827 cm^{-1} [83]. In the IR spectral range there is only a broad asymmetric band due to absorption of OH-groups dissolved in the melt during the glass melting. Appearance of a small amount of ZnO nanocrystals, see Fig. 7(c), leads to a pronounced change in the absorption spectrum of the sample. Absorption edge is shifted to longer wavelengths, the band with a maximum at ~630 nm increases in intensity. A close look at this band reveals two additional maxima at 597 and 654 nm, see Fig. 7(b). In the assignment of this absorption spectrum, we referred to the paper of B. Babu *et al.* [84], wherein the optical absorption spectrum of Cr^{3+} doped ZnO nanopowder was presented. The authors confirmed that the Cr^{3+} in

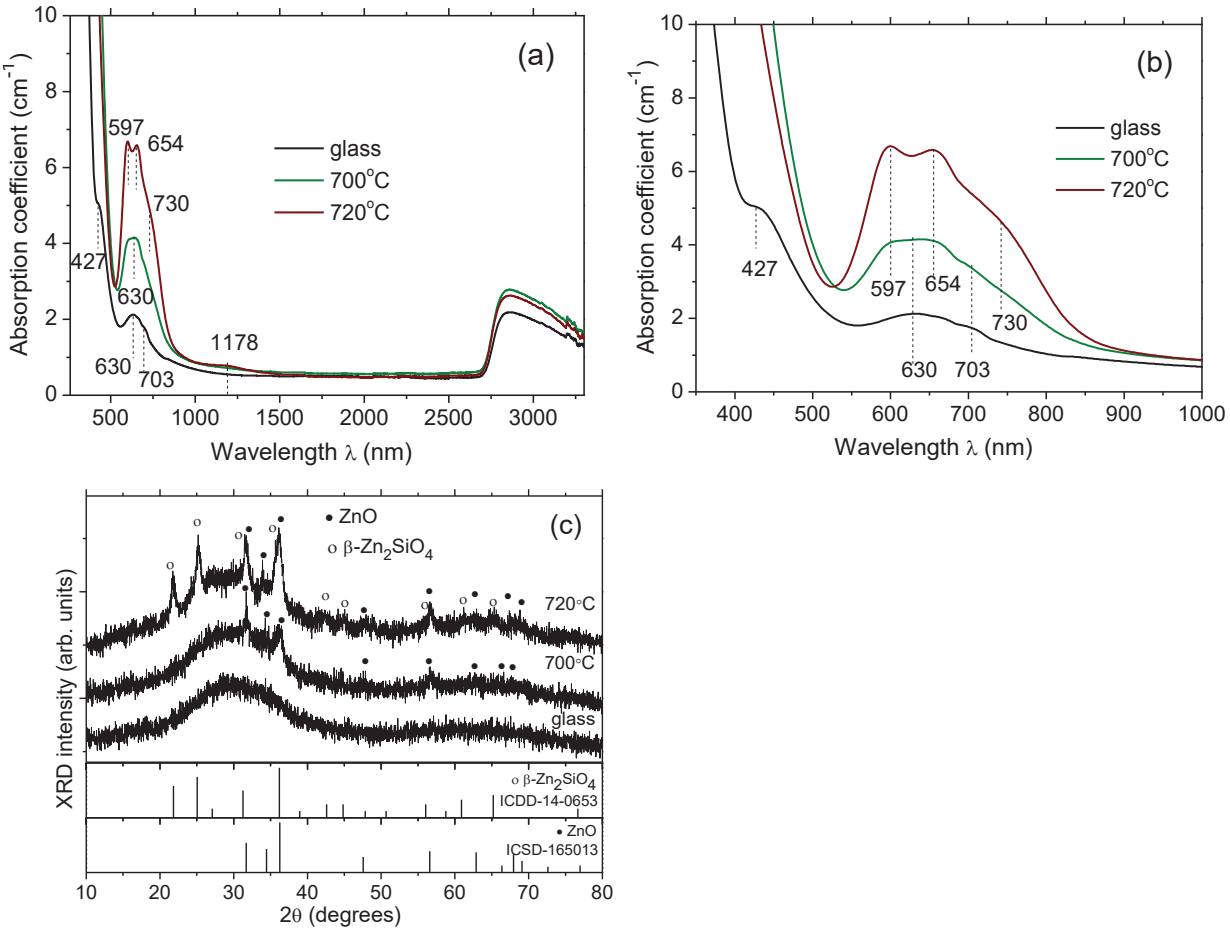

Figure 7. Absorption spectra of the initial and heat-treated glass Zn1 doped with 0.1 mol% Cr_2O_3 (a,b) in the spectral range of 260 – 3300 nm (a), in the spectral range of 350 – 1000 nm (b) Absorption spectra (a,b) and corresponding XRD patterns (c) of the initial and heat-treated glass Zn1. The standard XRD patterns of ZnO and β-Zn_2SiO_4 are presented. Heat-treatment temperatures are listed in the figure. Heat-treatment time is 2 h.

ZnO crystals are in octahedral site symmetry in the host ZnO lattice. Two bands observed at 426 nm and 588 nm were assigned to the transitions $^4A_{2g}(F) \rightarrow {}^4T_{1g}(F)$ and $^4A_{2g}(F) \rightarrow {}^4T_{2g}(F)$,respectively. The weak absorption band observed at 702 nm was attributed to the spin forbidden transition $^4A_{2g}(F) \rightarrow {}^2E_g(G)$. The ligand field parameters were determined as Dq = 1700 cm^{-1}, and B = 636 cm^{-1}. Based on these findings, we assigned the peaks in the spectrum of glass-ceramic prepared at 700 °C for 2 h to absorption of Cr^{3+} ions distributed between the octahedral sites in the ZnO crystals and in the residual glass.

Glass-ceramic sample prepared by the heat-treatment at 720 °C for 2 h is a three-phase material as it contains the crystals of ZnO and β-willemite distributed within the residual glass, see Fig. 7(c). The absorption spectrum of the glass-ceramic changes pronouncedly as compared with the spectrum of glass-ceramic prepared by the heat-treatment at 700 °C for 2 h: the intensity of the absorption band rapidly increases while its shape changes, see Fig. 7(b). There are two peaks with maxima at 597 and 654 nm, the inflection at ~730 nm and a weak peak at 1178 nm, see Fig. 7(a,b). This spectrum is also assigned to Cr^{3+} ions in octahedral site symmetry and shows two bands centered at 420 nm (concealed behind the absorption edge) and 590 nm that

arise from the spin allowed electronic transitions from $^4A_2 \rightarrow {}^4T_1$ and $^4A_2 \rightarrow {}^4T_2$, respectively and the spin forbidden transitions from $^4A_2 \rightarrow {}^2T_1$ and $^4A_2 \rightarrow {}^2E$ at 654 nm and 730 nm, respectively [85]. It should be mentioned that the spectra of Cr^{3+} in ZnO- and β-willemite-based glass-ceramics closely resemble those in Cr^{3+}-doped $MgAl_2O_4$ [86] and Cr^{3+}-doped $ZnAl_2O_4$ [87], wherein Cr^{3+} ions are six-fold coordinated. In ref. [85] it was stated that Cr^{3+} has a very low solubility in Zn_2SiO_4 and that additional spinel phases are easily formed. So we demonstrated difficulty in incorporation of octahedrally coordinated TM ions into the structure of ZnO crystals. In future, the detailed XRD analysis should be conducted to reveal if the secondary spinel phases are formed in these glass-ceramics.

These findings confirm the statement of L. Pinckney that "*Transition metal ions do partition into the tetrahedral sites of ZnO in these glass-ceramics [40]*.

3.1.5. Study of ZnO-based glass-ceramics doped with RE ions

Initial Zn2 glasses co-doped with Er_2O_3 and Yb_2O_3 are rose colored, coloration intensifies with increasing the Er doping concentration. The center of the glass co-doped with 0.2% Er_2O_3 and 0.2% Yb_2O_3 has a slightly yellow coloration, see Fig. 8.

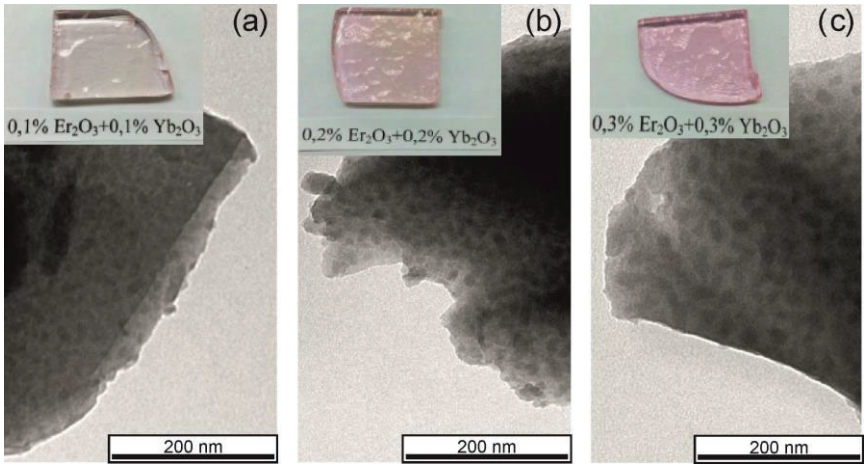

Figure 8. TEM images and photographs of initial Zn2 glasses doped with (a) 0.1% Er_2O_3 and 0.1% Yb_2O_3; (b) 0.2% Er_2O_3 and 0.2% Yb_2O_3; (c) 0.3% Er_2O_3 and 0.3% Yb_2O_3.

The TEM images of these glasses, Fig. 8(a-c), reveal a near-uniform distribution of dark regions of inhomogeneity, which confirms the phase separation for all examined initial glasses. From the comparison of their XRD patterns and absorptions spectra, Fig. 9, it follows that the doping level of RE^{3+} ions drastically influences the glass structure. An addition of 0.2/0.2 mol% Er_2O_3/Yb_2O_3 provokes crystallization of ZnO, which causes the location of the absorption edge at about 380 nm. The glasses co-doped with 0.1/0.1 and 0.3/0.3 mol% Er_2O_3/Yb_2O_3 are amorphous and liquid phase separated, see Fig. 9(a). However, a striking difference in the position of absorption edges in their absorption spectra, see Fig. 9(b), reflects different compositions of these regions. We speculate that in the glass doped with 0.1/0.1 mol% Er_2O_3/Yb_2O_3 amorphous regions of inhomogeneity are enriched in ZnO while the introduction of 0.3/0.3 mol% Er_2O_3/Yb_2O_3 leads to segregation of RE^{3+} ions into the phase-separated regions that results in diluting the Zn content and retarding the ZnO crystallization. Doping of the glass with different concentrations of Er_2O_3 and Yb_2O_3 modifies the kinetics of crystallization of ZnO.

Transparent glass-ceramics obtained by the heat-treatment at 720 °C contain ZnO nanocrystals, the sample doped with 0.2/0.2 mol% Er_2O_3/Yb_2O_3 has the highest fraction of ZnO.

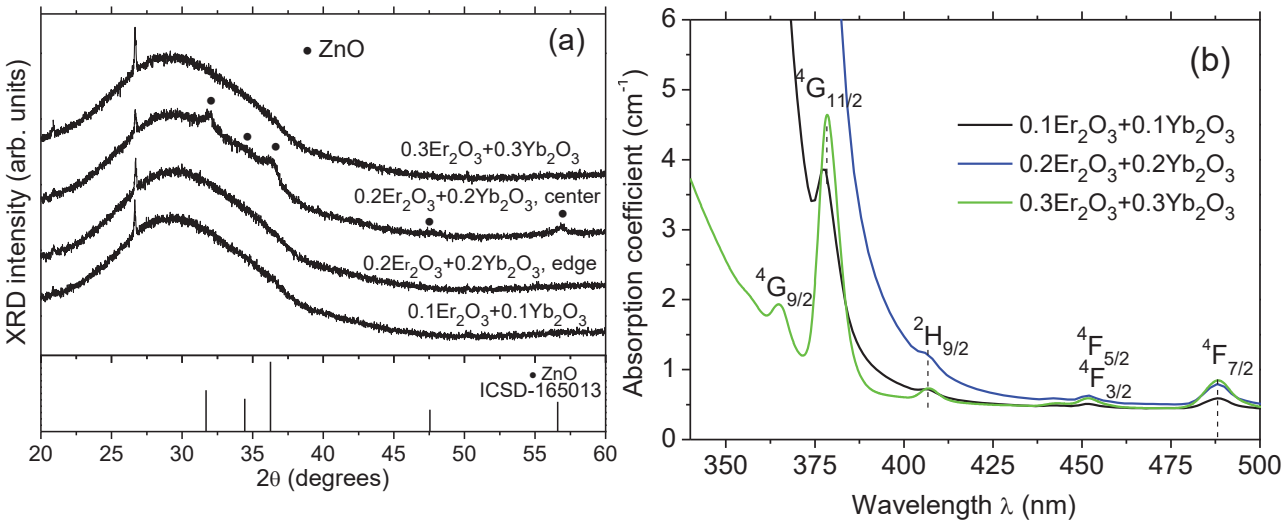

Figure 9. XRD patterns (a) and absorption spectra (b) of the initial Zn2 glasses co-doped with Er_2O_3 and Yb_2O_3. The standard XRD pattern of ZnO is presented. The Er_2O_3 and Yb_2O_3 doping level (mol%) is indicated in figure.

To estimate the effect of crystallization on spectral properties of ZnO-based glass-ceramics doped with RE_2O_3, we analyzed the difference between optical densities of samples of the heat-treated and initial glasses with approximately the same thickness h for a number of heat treatments. The analysis of the difference allowed us to exclude the reflection losses because the change in reflection caused by crystallization was estimated to be negligible. The difference between the optical density D_{GC} of the heat-treated (glass-ceramic, GC) sample and the optical density D_{IG} of the initial glass sample was used for the estimation of the extinction coefficient

$$\alpha_{ZnO} = (D_{GC} - D_{IG})/(h \log_{10} e) \cong 2.3026\,(D_{GC} - D_{IG})/h \qquad (5)$$

related to scattering and absorption originated from ZnO nanocrystals.

Three effects of ZnO crystallization on extinction coefficient α_{ZnO} of glass-ceramics doped with RE ions were demonstrated. First, ZnO nanocrystals cause a significant scattering of visible light. Second, the absorption band at long wavelengths (λ > 1000 nm) was observed which is related to the presence of free carriers in semiconductor ZnO nanocrystals [79] and is generally discussed in terms of localized surface plasmon resonance (LSPR). Finally, a fine effect of the changes in intensities and positions of Er^{3+} and Yb^{3+} absorption peaks was demonstrated for the first time using the analysis of difference of optical densities (Eq. (5)). Namely, we found that the changes in intensities and positions of Er^{3+} and Yb^{3+} absorption peaks in the course of the ZnO crystallization are observed for a number of concentrations of Er_2O_3 and Yb_2O_3 in the interval 0.05–2.0 mol% (including mixed compositions $x(Er_2O_3 + Yb_2O_3)$, x=0.2–1.0 mol%).

For illustration, the full absorption spectra and the extinction coefficients α_{ZnO} in vicinity of two absorption peaks of glass-ceramics containing (0.3 mol% Er_2O_3 + 0.3 mol% Yb_2O_3) are presented in Fig. 10(a-c). The corresponding XRD patterns are demonstrated in Fig. 10(d). The

unit cell parameters *a* and *c* and average sizes of ZnO crystals in glass-ceramics obtained by different heat-treatments are listed in Table 1.

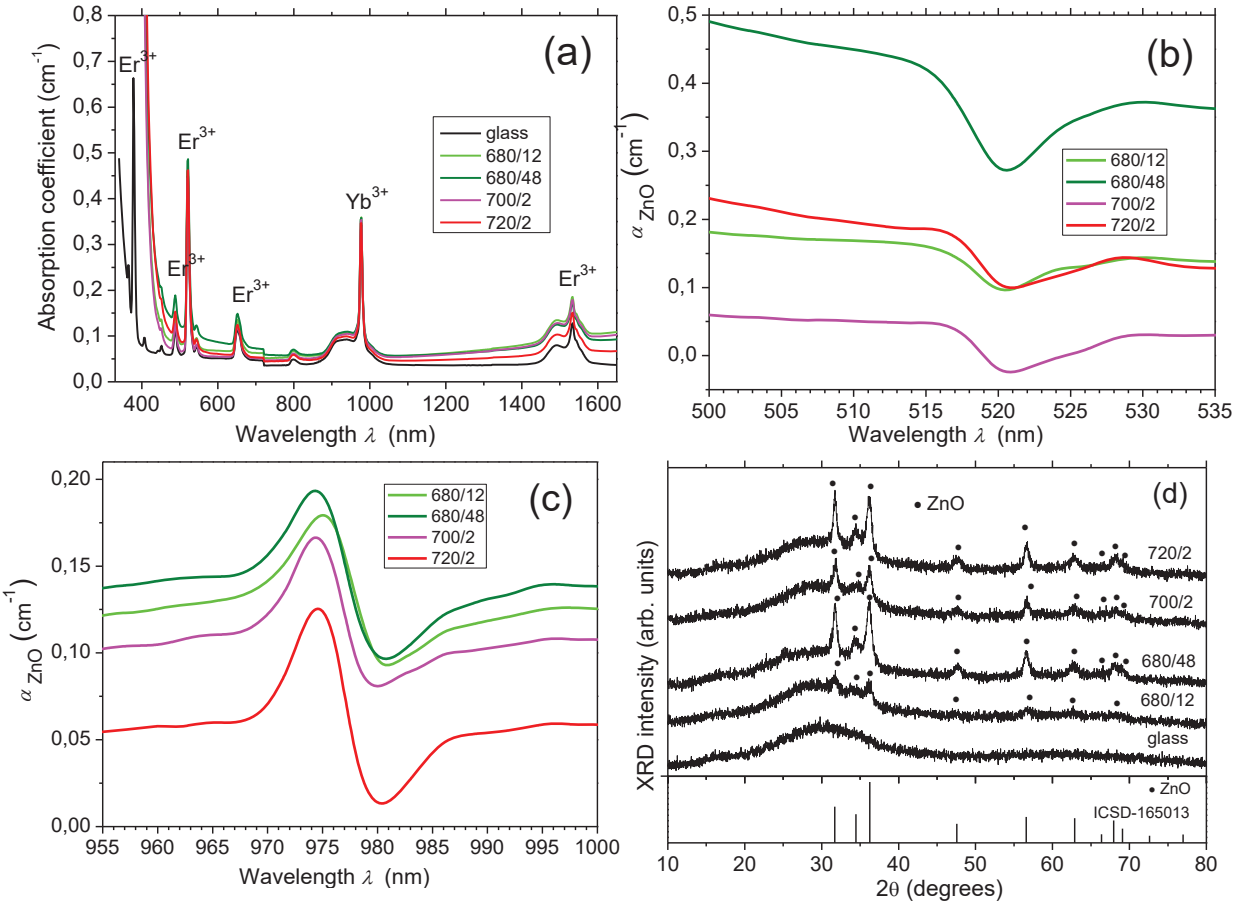

Figure 10. (a) Absorption spectra; (b,c) the extinction coefficient α_{ZnO} in the spectral ranges around the absorption peaks of Er^{3+} ($\lambda \cong 520$ nm) (b) and Yb^{3+} ($\lambda \cong 978$ nm) (c); (d) the corresponding XRD patterns of the initial and heat-treated glasses containing (0.3/0.3 mol% Er_2O_3/Yb_2O_3). The standard XRD pattern of ZnO is presented. Heat-treatment schedules, °C/h, are listed in the figure.

Table 1. The unit cell parameters and average sizes of ZnO crystals in glass-ceramics containing (0.3/0.3 mol% Er_2O_3/Yb_2O_3) and obtained by different heat-treatments.

Heat-treatment schedule, °C / h	The ZnO unit cell parameters (Å)		The average size of ZnO crystals (nm)
	a (±0.003)	*c* (±0.003)	
680/12	traces	traces	10.0
680/48	3.255	5.229	13.5
700/2	3.256	5.227	17.0
720/2	3.256	5.227	17.0

Fig. 10(b) shows that crystallization does not significantly change the position of the Er^{3+} absorption peak at $\lambda \cong 520$ nm whereas it appreciably reduces the intensity of this peak for all heat-treatments. The intensity of the absorption peak of Yb^{3+} ($\lambda \cong 978$ nm) does not change significantly due to crystallization while this peak is shifted to short wavelengths (Fig. 10(c)) for all heat-treatments. It means that the surrounding of RE ions slightly differs in the initial glass

and the glass-ceramics based on ZnO nanocrystals and it is influenced by crystallization of ZnO. The spectra of visible Er^{3+} luminescence of the initial glass doped with 0.1/0.1 mol% Er_2O_3/Yb_2O_3 and glass-ceramics based on ZnO nanocrystals and obtained by its heat-treatments at 700–800 °C were presented in [66]. The excitation wavelength was 488 nm. With the heat-treatment, the luminescence intensity gradually decreased while the shape of the emission bands did not change. This indicates that the Er^{3+} ions do not enter into the ZnO nanocrystals and remain in the residual glassy phase until the heat-treatment temperature of at least 800 °C. The observed decrease of the luminescence intensity can be explained by quenching of Er^{3+} luminescence in the residual glassy phase the volume of which decreases with the heat-treatment. The conclusion about location of RE ions in the residual glass is indirectly confirmed by the XRD pattern of the glass-ceramic prepared by the heat-treatment at 1300 °C for 2 h (Fig. 11). The XRD pattern exhibits diffraction maxima at 2θ=28.20° and 28.80° with almost similar intensities and a maximum at ~ 28.5° with a low intensity. Their appearance is connected with crystallization of RE silicate, orthorhombic phase $(Er,Yb)_2Si_2O_7$ (space group: *Pna2₁*), which corresponds to the ICDD card No. 82-0732.

Crystals containing RE ions were found in other RE-doped glass-ceramics prepared at high temperatures of 1200 - 1300 °C. Diffraction peaks of the crystals are well manifested in the angular range of 2θ = 27° - 32°. Identification of crystalline phases containing RE ions revealed that in Er-containing glasses Er_2O_3 crystals evolved at high temperatures, and Yb_2SiO_5 crystals were detected in glass-ceramics doped with ytterbium ions. A decrease in in the concentration of rare-earth ions below 1% leads to the crystallization of $Er_2Si_2O_7$ and $Yb_2Si_2O_7$. Thus, we came to conclusion that Re^{+3} ions are located in the glass phase and during high-temperature secondary heat-treatments interact with silica of this residual glass with the formation of RE silicates.

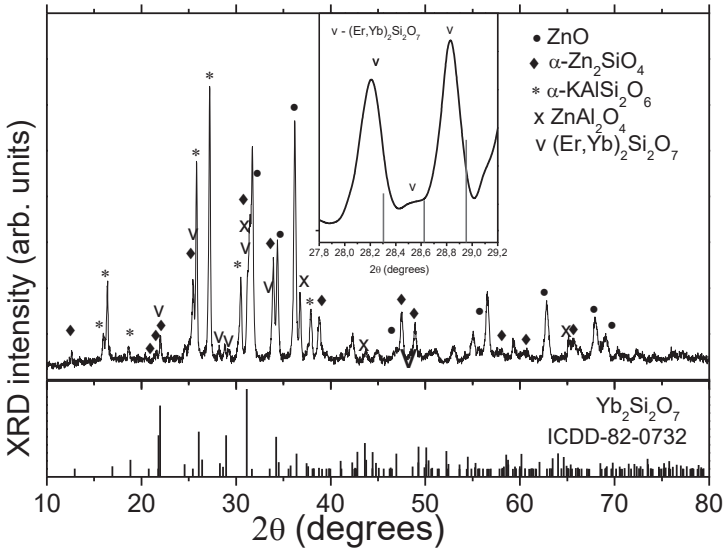

Figure 11. The XRD pattern of the glass-ceramic doped with 0.1 mol% Er_2O_3 and 0.1 mol% Yb_2O_3 prepared by the heat-treatments at 1300 °C for 2 h. The standard XRD pattern of $Yb_2Si_2O_7$ is presented. Insert presents the part of this pattern recorded in a scanning mode (2θ=27.6–29.8°) with 100 s exposure time.

These findings confirm the statement of L. Pinckney that "*Large rare earth ions are unlikely to enter the ZnO crystals and would remain in the residual glass phase after crystallization" [40].*

3.2. Ceramics

3.2.1. Ceramics doped with RE ions

3.2.1.1. XRD analysis of ceramics

Typical XRD patterns of RE-doped ZnO ceramics are shown in Figure 12(a) by an example of the ZnO:5.0 wt% Er sample and in Figure 13(a) by an example of the ZnO: 1/4 wt% Er/Yb sample. All the XRD patterns of the ZnO:Yb, ZnO:Er and ZnO:(Er,Yb) transparent ceramics evidence crystallization of hexagonal (sp. gr. $P6_3mc$) phase of ZnO with wurtzite structure and RE_2O_3 with a cubic (sp. gr. $Ia\bar{3}$) C-type bixbyite structure. The calculated ZnO unit cell parameters for the ZnO:Yb, ZnO:Er and ZnO:(Er,Yb) ceramics nearly coincide with those for the undoped ZnO (a = 3.249 Å, c = 5.205 Å, ICSD card No. 165013). They do not change with increasing the RE content from 0.2 to 5.0 wt%, which indicates that RE^{3+} ions do not enter the ZnO structure under the conditions used for the manufacture of ceramics (HPing of

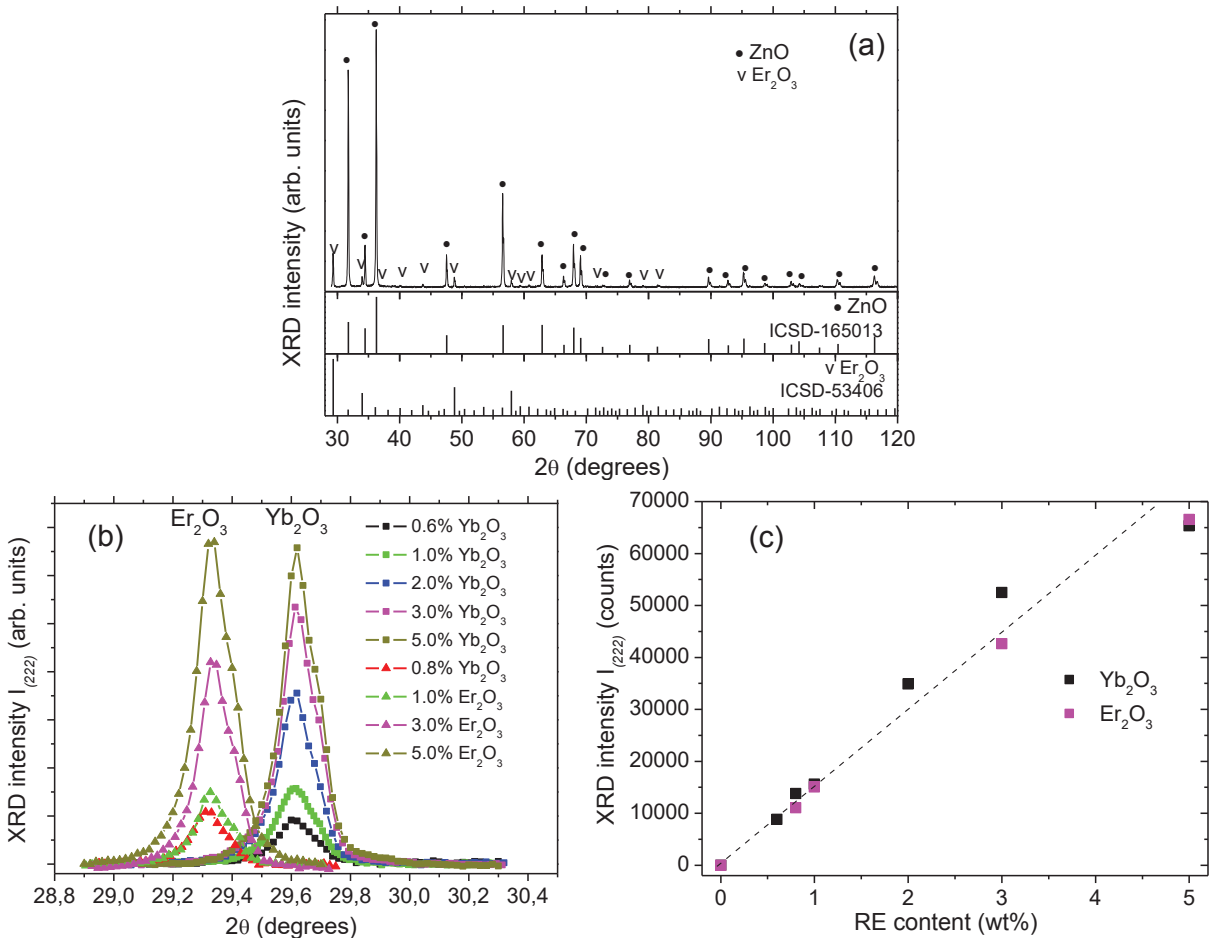

Figure 12. (a) XRD pattern of ZnO:5 wt% Er optical ceramic and standard XRD patterns of ZnO and Er_2O_3; (b) XRD patterns of ZnO:RE ceramics with different Er and Yb doping levels in the 2θ range of 28.9–30.3° corresponding to (222) peaks of Er_2O_3 and Yb_2O_3; (c) the dependence of the corresponding peak diffraction intensity at 2θ of 29.33° and 29.63° on the RE content.

mechanically mixed powders of reagents at temperatures of 1150 - 1180 °C).

The fragments of the XRD patterns in the range of diffraction angles 2θ of 29.0 - 30.3° contain intense diffraction peaks of Er_2O_3 and Yb_2O_3 with the Miller's index (*hkl*) = (222), Figs 12(b) and 13(b). The volume fraction of RE_2O_3 crystals in ceramics gradually increases with RE content, Fig. 12(c). The calculated unit cell parameters of RE_2O_3 are independent of the RE content in ceramics. The unit cell parameter of Yb_2O_3 a = 10.441±0.003 Å, that of Er_2O_3, a = 10.545±0.003 Å. The size of RE_2O_3 crystals in ZnO:RE ceramics is also independent of the dopant concentration; the average size of Yb_2O_3 crystals is ~70 nm, the average size of Er_2O_3 crystals is ~76 nm.

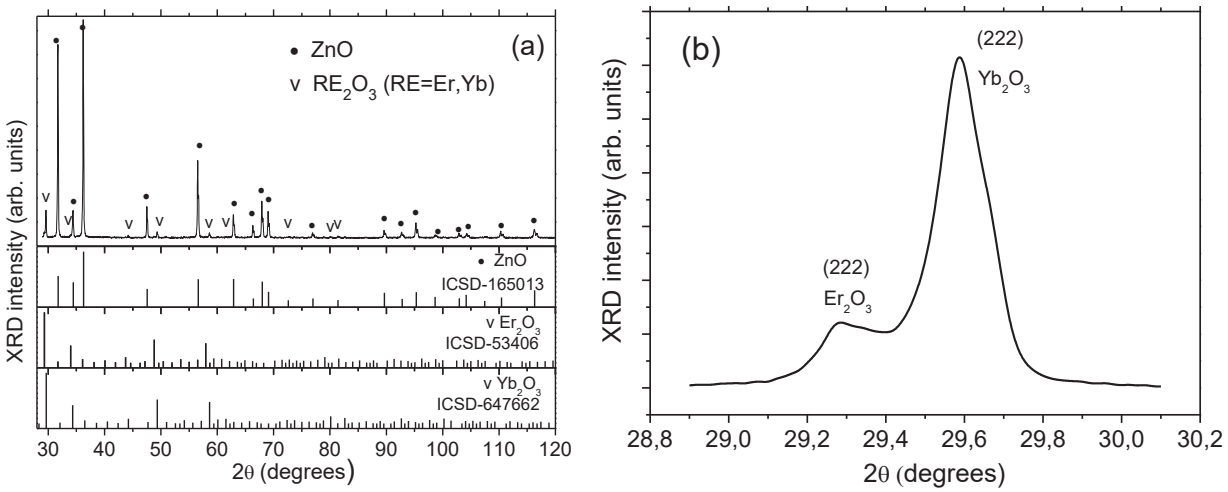

Figure 13. (a) XRD pattern of ZnO:1/4 wt% Er/Yb and standard XRD patterns of ZnO, Er_2O_3 and Yb_2O_3; (b) XRD pattern of ZnO:1% Er /4% Yb ceramic in the 2θ range of 28.9–30.3° corresponding to (222) peaks of Er_2O_3 and Yb_2O_3.

3.2.1.2. Texture characterization of ceramics.

The uniaxial pressing conditions used for the manufacturing of ZnO transparent ceramics inevitably result in texture appearance, i.e., in a predominant orientation of crystal grains. The texture coefficient is a parameter that allows estimating the contribution of different planes of ZnO crystals to the texture formation, see Eq. (1). The reflections from the planes of a hexagonal prism have Miller's indices (100) and (110), the reflections from a pedion have the (002) indices, and those from a hexagonal pyramid have the (101) and (102) indices. For the undoped ZnO ceramic, the texture is dominated by the (100) and (110) prism planes of the ZnO crystals [88,89]. For the ceramics containing RE ions, the prism planes with (*hkl*) = (100) and (110) and the shallow pyramid (101) dominate. These texture changes can be assigned to localization of RE ions on the active faces of the ZnO crystals [89].

3.2.1.3. Morphological characterization of ceramics

The surface morphology of ceramics was characterized by SEM, see Fig. 14, that shows typical SEM images of an etched polished surface of the 0.4 wt% Er-doped transparent ZnO ceramic as an example.

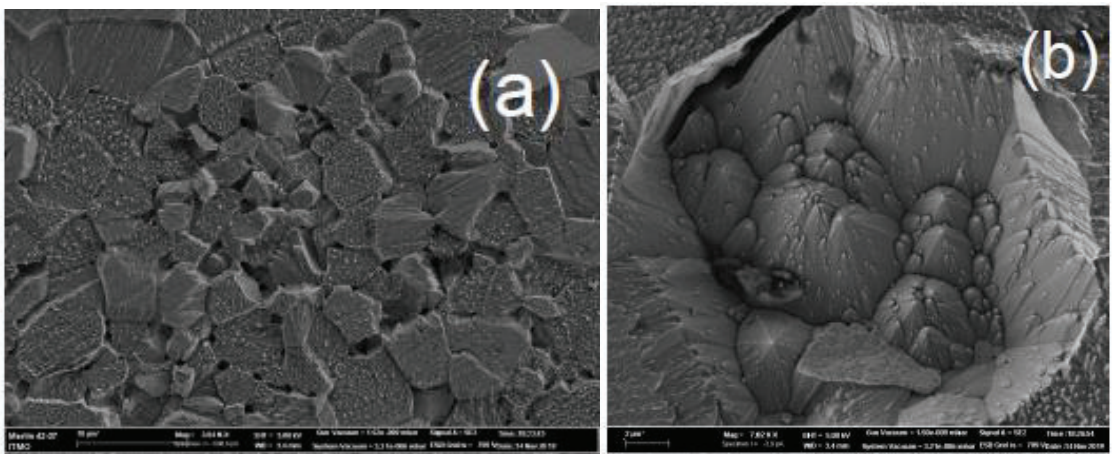

Figure 14. SEM images of the polished surface of 0.4 wt% Er-doped ZnO ceramic. The scale bars are (a) 10 μm and (b) 2 μm.

The powder HIPing occurs along thermodynamically favorable crystal planes. The images demonstrate grain surfaces with different orientations. They are the faces of the prism and pedions with characteristic growth hillocks in the form of hexagonal pyramids [89]. The microstructure of the ZnO:0.4 wt% Er ceramic presented in Fig. 14(a,b) is characteristic of all the ceramics under study. The sizes of the resulting grains are not uniform. It is reasonable to assume that larger grains are built of ZnO, while the small grains can be attributed to RE_2O_3 crystals. The variation of the type of RE element (Er or Yb), its concentration, the source of the RE_2O_3 reagent and the HPing temperature do not influence the surface morphology of ZnO:RE crystals. Note that synthetic ZnO single crystals demonstrate similar morphology as the hexagonal prism, the pedion, and the hexagonal pyramid are simple forms characteristic for hexagonal ZnO crystals belonging to the 6*mm* point group [11,12]. Located on the crystal faces, and not entering the zinc oxide structure, Er and Yb doping ions have an inhibitory effect on the grain growth of ZnO ceramics. The addition of RE ions significantly, (almost four times, from 23.0 to 7.0 μm) reduces the average grain size of ZnO ceramics prepared at the same HPing temperature of 1150 °C [89].

3.2.1.4. The microstructure and compositional analysis of the ZnO and ZnO:Er,Yb ceramics

By the example of the ZnO:5.0 wt% Yb, ZnO:2.0 wt% Er and ZnO:0.6/0.8 wt% Er/Yb samples, the SEM-EDX analysis of the ZnO:RE optical ceramics reveals their multiphase composition, see Fig. 15. They are composed of ZnO, Er_2O_3 and Yb_2O_3 microcrystals. A tight contact between microcrystals of RE_2O_3 and larger ZnO crystals ensures an effective interaction on the interface of these crystals and results in modification of the spectral-luminescent properties of the ZnO optical ceramics doped with RE ions [88,89].

3.2.2. Ceramics doped with cobalt ions

3.2.2.1. XRD analysis of ceramics

We made the first attempts to prepare ZnO optical ceramics doped with cobalt ions. The selected Co concentrations were 0.1, 0.5, 1.0 and 5.0 wt%. A typical XRD pattern is shown in the example of the ZnO:1 wt% Co ceramic, see Fig. 16(a). The pattern demonstrates diffraction

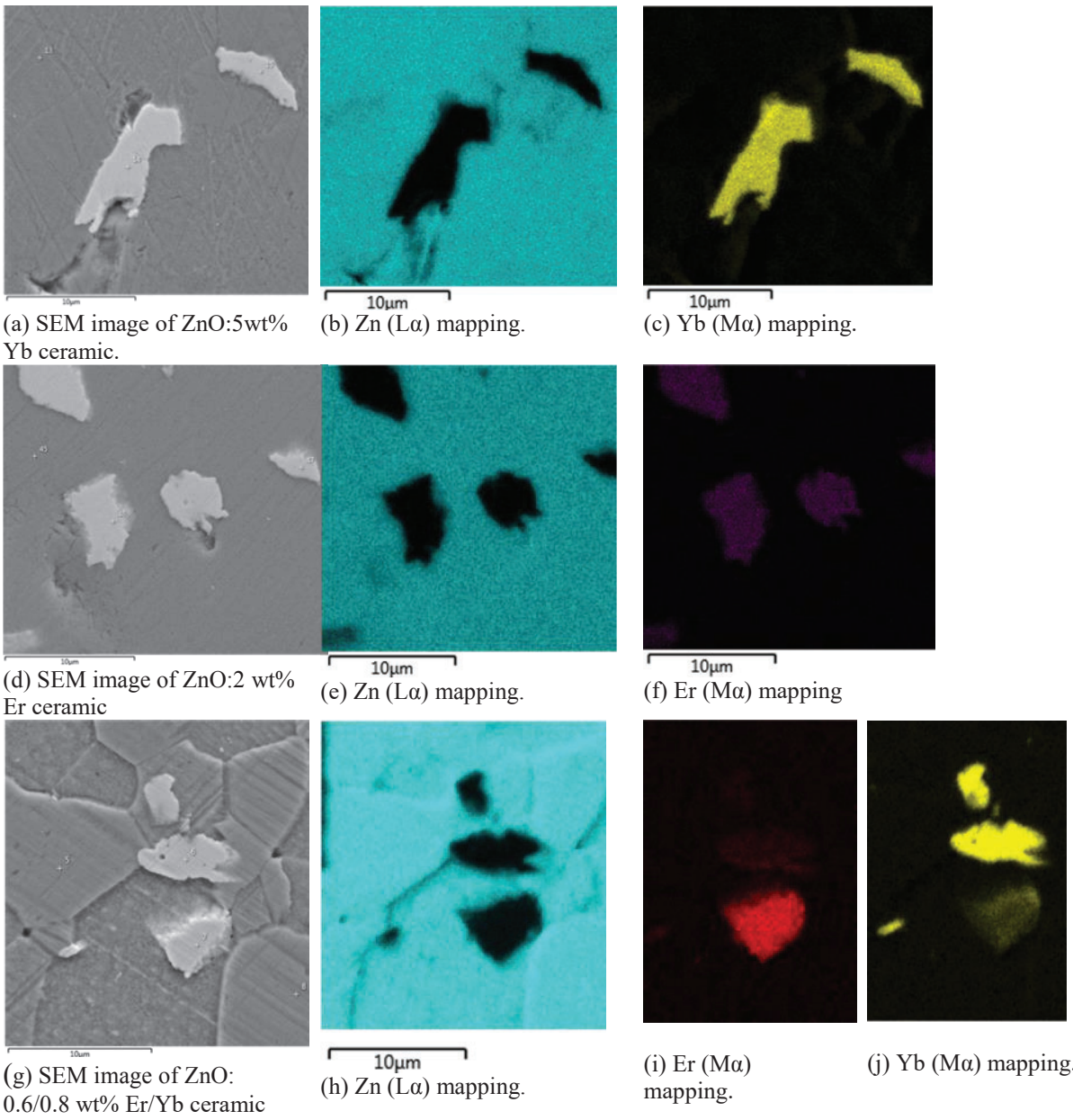

(a) SEM image of ZnO:5wt% Yb ceramic. (b) Zn (Lα) mapping. (c) Yb (Mα) mapping.

(d) SEM image of ZnO:2 wt% Er ceramic (e) Zn (Lα) mapping. (f) Er (Mα) mapping

(g) SEM image of ZnO: 0.6/0.8 wt% Er/Yb ceramic (h) Zn (Lα) mapping. (i) Er (Mα) mapping. (j) Yb (Mα) mapping.

Figure 15. (a,d,g) SEM images of the polished and etched surface of the ZnO:RE ceramics; (b,c,e,f,h-j) EDX element mapping of (b,e,h) Zn (Lα), (c,j) Yb (Mα) and (f,i) Er (Mα). (a-c) the ZnO:5 wt% Yb ceramic; (d-f) ZnO:2 wt% Er ceramic; (g-j) ZnO:0.6/0.8 wt% Er/Yb ceramic.

peaks corresponding to all the planes of the hexagonal phase of ZnO, ISDD #5-0664, and additional peaks located at 2θ = 42.30, 61.42, and 73.99°, see Fig. 16(a,b). These peaks correspond, respectively, to (200), (220), and (311) planes of face-centered cubic CoO, *Fm3m*, JCPDS #78-0431.

With increasing the cobalt concentration, the unit cell parameters of ZnO crystals remain near unchanged, and their values practically coincide with those indicated in the literature (a = 3.249 Å, c = 5.205 Å, ISDD card No. 5-0664). The fraction of CoO crystals in ZnO:Co ceramics increases in proportion to the concentration of the Co reagent, Co_3O_4. It is possible to trace the growth of the CoO crystal fraction by an increase of intensity of the diffraction peak located at 2θ = 42.30° and corresponding to the (200) plane of the CoO crystal. At doping with 0.5 wt% Co, the peak (200) on the XRD pattern is not detected. It appears when the Co content is

Table 2. The unit cell parameters ZnO and CoO crystals in ZnO: 1.0 wt% Co ceramic

CoO content, wt%	The ZnO unit cell parameters (Å)		The CoO unit cell parameter (Å)
	a (±0.003)	*c* (±0.003)	*a* (±0.003)
0.5	3.253	5.204	-
1.0	3.251	5.203	4.267
5.0	3.254	5.207	4.267

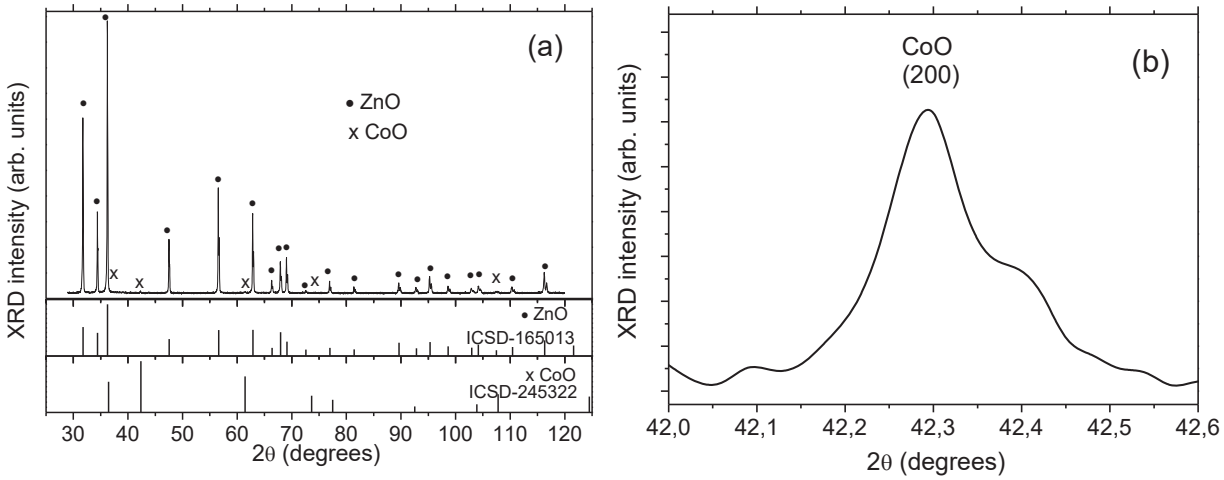

Figure 16. (a) XRD pattern of the ZnO:1 wt% Co ceramic and the standard XRD patterns of ZnO and CoO; (b) XRD pattern of ZnO:1 wt% Co ceramic in the 2θ range of 42.0 - 42.6° corresponding to the (200) peak of CoO.

1.0 wt%, and it increases in the XRD pattern of ZnO: 5.0 wt% Co ceramic. The CoO unit cell parameter *a* in ceramics does not change with increasing the Co doping level, see Table 2. The value of the parameter *a* = 4.267 Å is similar to that of pure CoO (*a*=4.262 Å, JCPDS #78-0431) though it is possible to expect the formation of solid solution between CoO and cubic ZnO with the rock salt structure (S.G. *Fm3m, a*=4.280 Å, JCPDS #77-0191).

3.2.2.2. The microstructure and compositional analysis of the ZnO:Co ceramics

The microstructure of ZnO:Co ceramics is composed of grains of various shapes and sizes, see Fig. 17(a) as a typical image. Along with isometric grains, which are characteristic for undoped ZnO ceramic, the grains of rectangular shape are observed. The length of grains somewhat increases with the Co doping level. The grain size varies from 5-7 to 25-30 μm.

Fig. 17(b) presents the backscattered electron image (at low accelerating voltage) of the surface of ZnO:0.5 wt% Co ceramic. The numbers 1-3 mark the dark regions of irregular shape with sizes of 10 to 20 μm. According to the SEM-EDX data, these three regions as well as other dark regions not shown here have the same composition and contain ~36 at% Co, 20 at% Zn, and 44 at% O. The composition of the main part of the ceramic was determined in different regions of the sample. The content of Zn and O is found to be near constant when analyzed in different parts

of the sample, while the Co content varies from 0.05 to 0.2 at%. For instance, the region denoted by the number 4 has the composition of ~54 at% Zn, ~46% O and contains 0.03 at% Co.

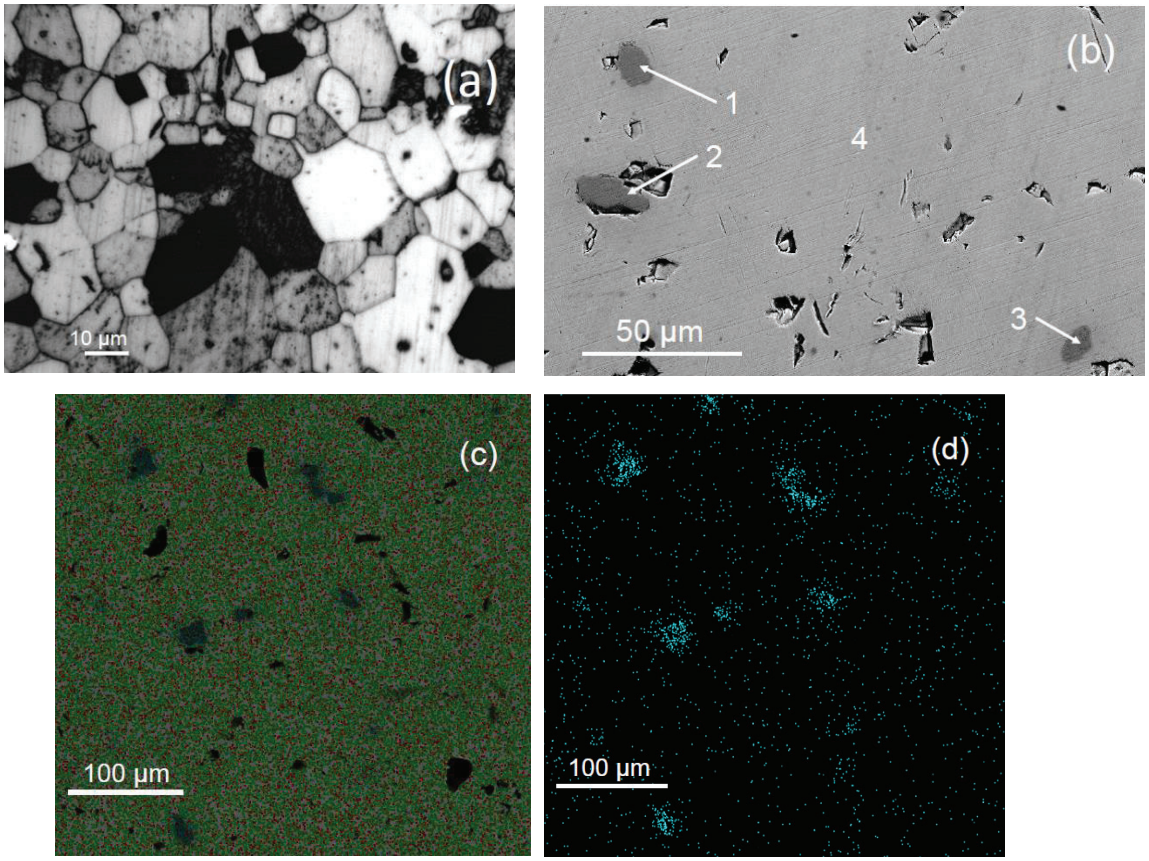

Figure 17. (a,b) Micrograph of the etched surface(a) and the backscattered electron image (b) of the ZnO:0.5 wt% Co ceramic; (c,d) EDX Zn, O, and Co element mapping (c) and Co element mapping (d) of the ZnO:1 wt% Co ceramic.

These findings are confirmed by the SEM-EDX element mapping, see Fig. 17(c,d), where two types of cobalt ions localization are observed, i.e., the homogeneous distribution of Co atoms along the ZnO sample as well as their localization within the regions enriched in cobalt ions, which is in accordance with ref. [90].

3.2.2.3. Optical properties of the ZnO:Co ceramics

Figure 18(a,b) shows the absorption spectra of ZnO:Co ceramics with different doping concentrations. Absorption spectrum of ZnO:1 wt% Co ceramic in the spectral range of 300 – 3300 nm presents the characteristic features of Co^{2+} ions and ZnO crystals: there are the broad structured absorption bands of Co^{2+} ion in tetrahedral site symmetry position characteristic of these ions in ZnO crystals [74-76], and the absorption band at longer wavelengths ($\lambda > 1800$ nm) which is connected with the presence of free carriers in semiconductor ZnO crystals [79], see Fig. 18(a). Figure 18(b) shows that the absorption edge in the spectrum shifts to longer wavelengths, intensities of cobalt absorption bands increase, and the raise of absorption connected with the presence of free carriers shifts to longer wavelengths with the increase of doping concentration. The detailed analysis of the Co^{2+} spectrum was done based on the paper of

R. Pappalardo *et al.* [74] and refs [75,76]. The dominant absorption bands in the visible spectral range at 566, 610 and 653 nm were assigned as $^4A_2(^4F) \rightarrow {}^4T_1(^4P)$ and the bands in the IR at 1306, 1416, 1519, and 1644 nm were assigned as $^4A_2(^4F) \rightarrow {}^4T_1(^4F)$ transition due to the high spin d^7 electron configuration of the tetrahedrally coordinated Co^{2+} ions. We should bear in mind that according to XRD data presented above, ZnO:Co ceramics contain CoO crystals. Co^{2+} ions have octahedral coordination in CoO crystals with the rock salt structure [91]. The absorption spectrum of CoO is presented in Fig. 5 of the ref. [92]. It contains three bands, i.e. the rather narrow band at 357 nm attributed to ligand-metal charge transfer from O(II) to Co(II), the absorption centered at 550 nm and ascribed to Co(II) transitions in octahedral crystal field, and a very broad absorption in the near infrared centered at about 1000 nm and spanning up to 1200 nm. The absorption spectrum of octahedrally coordinated Co^{2+} ions in MgO [74] presents absorption bands in the visible and in the near infrared. R. Pappalardo *et al.* mention [74] that the

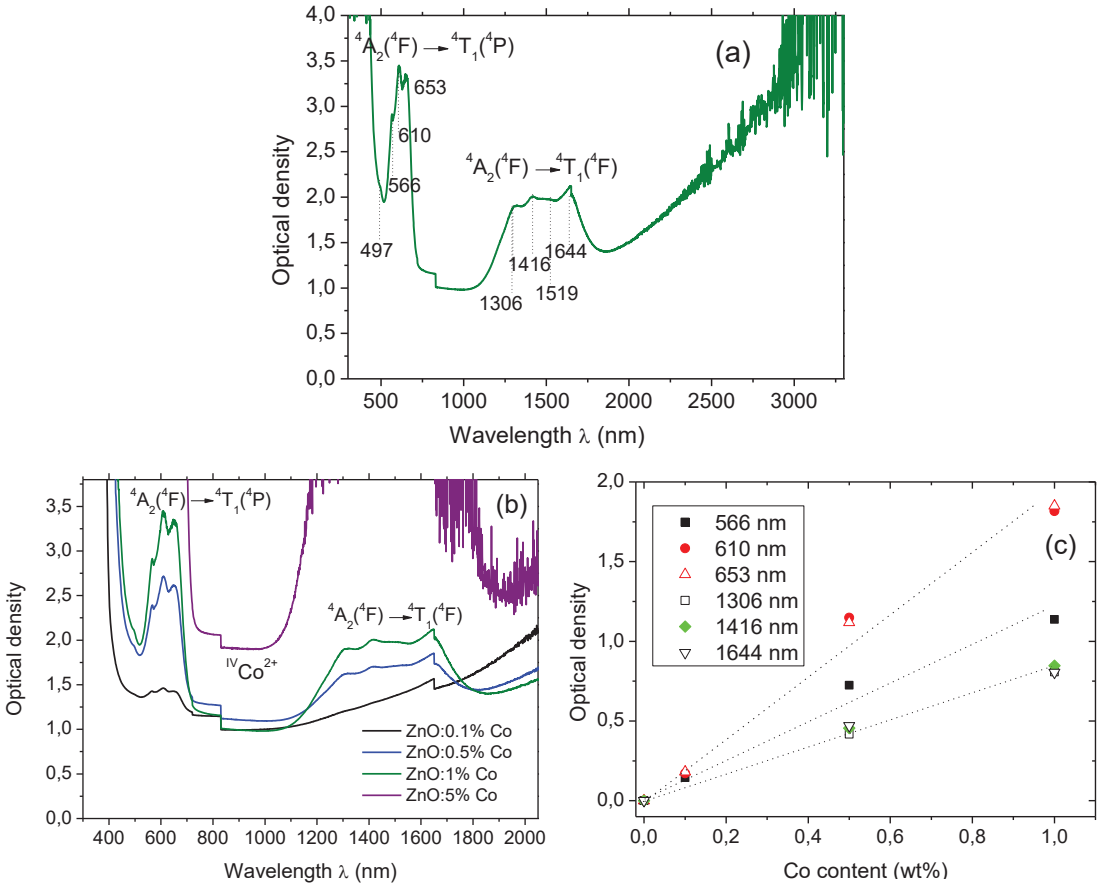

Figure 18. Absorption spectrum of ZnO:1 wt% Co ceramic in the spectral range of 300 – 3300 nm (a); absorption spectra of ZnO: Co ceramics doped with 0.1 – 5.0 wt.% Co in the spectral range of 300 – 2050 nm (b); the dependence of the optical density at 566, 610, 653, 1306, 1416, and 1644 nm on the Co content (c). The thickness of the samples is ~0.5 mm.

oscillator strength in tetrahedral coordination (ZnO:Co) is greater by a factor ~10^3 than for MgO:Co. Therefore, absorption caused by Co^{2+} ions in octahedrally coordinated CoO crystals come unnoticed in absorption spectra of ZnO:Co ceramic. According to Fig. 18(c), the Beer's law, i.e., a linear dependence between the concentration of Co^{2+} ions and the peak optical density (after subtracting the background losses), is fulfilled for all Co^{2+} peaks in the absorption spectra

of ceramics. It indicates that with increasing the Co concentration, new species do not appear, which allows us to conclude that the distribution of cobalt ions between the ZnO and CoO crystals is almost independent of the Co^{2+} concentration.

3.3. Comparison of glass-ceramics and ceramics

In this section, we compare the structure of glass-ceramics and ceramics based on ZnO. Previously, a comparative study of spinel-based ceramics and glass ceramics allowed us to elucidate the structural and spectral features of both materials [93,94].

The XRD pattern of the Zn1 glass-ceramic doped with 0.1% CoO reveals a multiphase material exhibiting the strongly broadened diffraction peaks of ZnO located at the same positions as for the ZnO ceramic, as well as a halo located at $2\theta \approx 29°$ due to a high content of the residual potassium aluminosilicate glass, see Fig. 19(a,b). A small ZnO crystal size and relatively low crystallinity fraction in glass-ceramic become evident from this comparison. The study of the phase composition of glass-ceramics containing 0.1 – 3% CoO did not reveal formation of CoO crystals. Consequently, the cobalt ions enter the ZnO crystals as isomorphic impurity. ZnO:Co ceramics are two-phase crystalline material, composed of ZnO crystals with a tiny fraction of CoO crystals.

The comparison of absorption spectra of cobalt-doped glass-ceramic and ceramic, Fig. 19(c), clearly indicates the presence of cobalt ions in one oxidation state, Co^{2+}, in the T_d (tetrahedral) sites. The shape of absorption bands and positions of absorption peaks caused by Co^{2+} ions in both materials coincide which implies that they both originate from T_d coordinated Co^{2+} ions in Zn^{2+} sites in ZnO crystals. As we mentioned in the previous section, absorption caused by Co^{2+} ions in octahedrally coordinated CoO crystals come unnoticed in absorption spectra of ZnO:Co ceramic because of its low oscillation strength. The optical losses in the mid IR spectral range in these materials have different origin: in glass-ceramic, the broad band with a maximum at about 2800 cm^{-1} is due to absorption of OH-groups dissolved in the glass during its melting; in ceramic, the IR absorption is y related to the presence of free carriers in semiconductor ZnO nanocrystals. Quite predictably, the transparency of nanophase glass-ceramic is much higher than that of ceramic.

The Raman spectra of the Zn2 glass-ceramics doped with 0.1 mol% Yb_2O_3 prepared by the heat-treatment at 750 °C for 2 h and of the ZnO:0.2 wt% Yb ceramic presented in Fig. 20 allowed us to reveal the characteristic features of both materials. In this comparison, we based on our interpretations of Raman spectra of glass-ceramics [71] and ceramics [89]. All characteristic vibrations of ZnO with wurtzite structure are observed in the Raman spectra of ZnO:0.2Yb ceramics at 99, 202, 331, ~379, 409, 437, 482, 539, 578, 663, 723, 743, 776, 812, 980, 1104 and 1150 cm^{-1}. Their assignment is presented in Table 3. Note that one of the most intense modes in the Raman spectrum of ZnO is a very narrow peak E_2^{low} at ~100 cm^{-1}, ascribed to vibrations of the zinc sublattice in ZnO [95], while another intense Raman mode E_2^{high} at~437 cm^{-1} is assigned to oxygen vibrations [95].

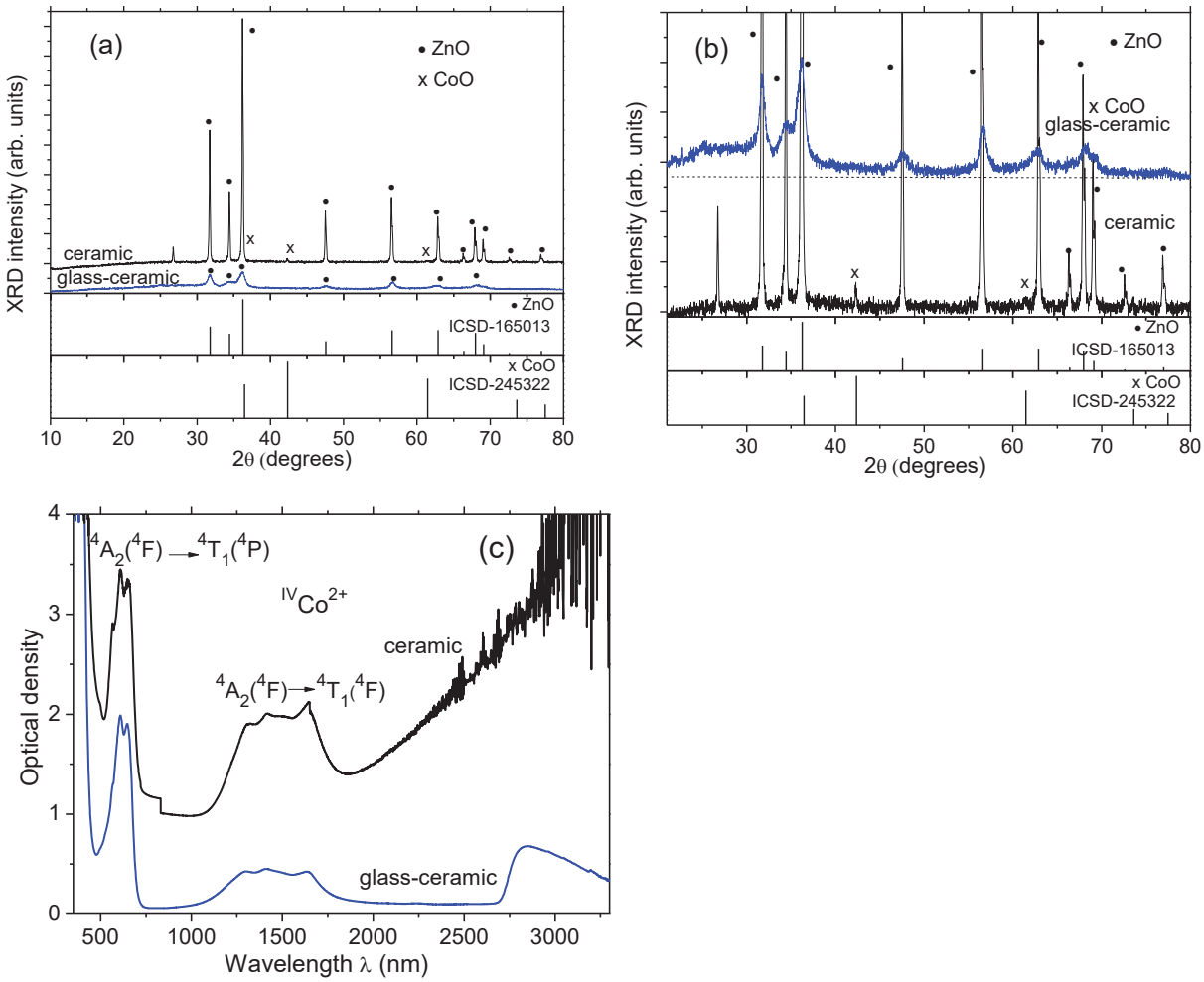

Figure 19. (a) XRD patterns of the Zn1 glass-ceramics doped with 0.1% CoO prepared by the heat-treatment at 750 °C for 2 h and the ZnO:1 wt% Co and the standard XRD (c) patterns of ZnO and CoO; (b) a close look on the XRD pattern of the same materials; the corresponding absorption spectra. The thickness of the glass-ceramic sample is 3 mm; the thickness of ceramic sample is 0.5 mm.

In the Raman spectrum of glass-ceramic previously we noticed only the most intense ZnO Raman modes. Now we can confirm that other modes are also found in the Raman spectrum of glass-ceramic. The most interesting finding is that the broad ZnO Raman modes at 1104 and 1150 cm^{-1} do exist in the spectrum of glass-ceramic. Indeed, the broad band with the maximum at 1104 nm is a result of superposition of vibrations within the aluminosilicate residual glass and the $2A_1(LO)$, $2E_1(LO)$ and 2LO modes of ZnO. The broad intense peaks at 482 and 578 cm^{-1} in the spectrum of glass-ceramic are assigned to vibrations within the aluminosilicate residual glass, though the weak modes of ZnO can also participate in these bands. Comparison of Raman spectra of glass-ceramics and ceramics not only elucidates a difference in phase composition of materials due to appearance of vibrations of aluminosilicate network of residual glass in the regions of ~480, ~580 and ~1000-1150 cm^{-1} in Raman spectra of glass-ceramics, but also allowed us for the first time to detect in this spectrum the modes of ZnO crystals localized in the region of 1100 - 1150 cm^{-1} , which are superimposed on the broad bands

due to vibrations of the aluminosilicate network of residual glass and could not be detected without this comparison.

Table 3. Frequencies of the Raman-active modes of ZnO in the ZnO:0.2 wt% Yb ceramic and Zn2 glass-ceramics doped with 0.1 mol% Yb_2O_3 prepared by the heat-treatment at 750 °C for 2 h in comparison with literature data.

Frequency, cm^{-1}			Symmetry	Process
Ceramic	Glass-ceramic	[95]	[95]	[95]
99	99	99	E_2	E_2^{low}
202		203	A_1, (E_2)	2TA; 2 E_2^{low}
331	331	333	A_1, (E_2, E_1)	E_2^{high} –E_2^{low}
379		378	A_1	A_1, (TO)
409		410	E_1	E_1 (TO)
437	437	438	E_2	E_2^{high}
482		483	A_1	2LA
539		536	A_1	$2B_1^{low}$; 2LA
578	578	574	A_1	A_1(LO)
663	663	666	A_1	TA+LO
723	723	723	A_1	LA+TO
743		745	A_1	LA+TO
776	781	773	A_1	LA+TO
812		812	A_1	LA+LO
980	980	980	A_1	2TO
1104	1104	1105	A_1	2LO
1150	1150	1158	A_1	$2A_1$(LO), $2E_1$(LO); 2LO

The difference in phase compositions of glass-ceramics and ceramics doped with RE ions is seen from the comparison of their XRD patters, see Fig. 21(a,b). Transparent glass-ceramics prepared by the heat-treatment at 750 °C for 2 h demonstrate a low ZnO crystallinity fraction of ~5 wt% and size of ~20 nm [79]. The ZnO crystals are distributed within the residual glass. The near completely crystallized glass-ceramics prepared by the heat-treatment at 1300 °C for 2 h contain oxide, silicate and aluminosilicate crystalline phases. It is quite interesting that RE ions are crystallized in different forms depending on the type and concentration of RE ion and the heat-treatment temperature. In the XRD patterns of glass-ceramics presented in Fig. 21(a,b) there are the crystalline phases of $Yb_2Si_2O_7$, $Yb_2Si\ O_5$, and Er_2O_3.

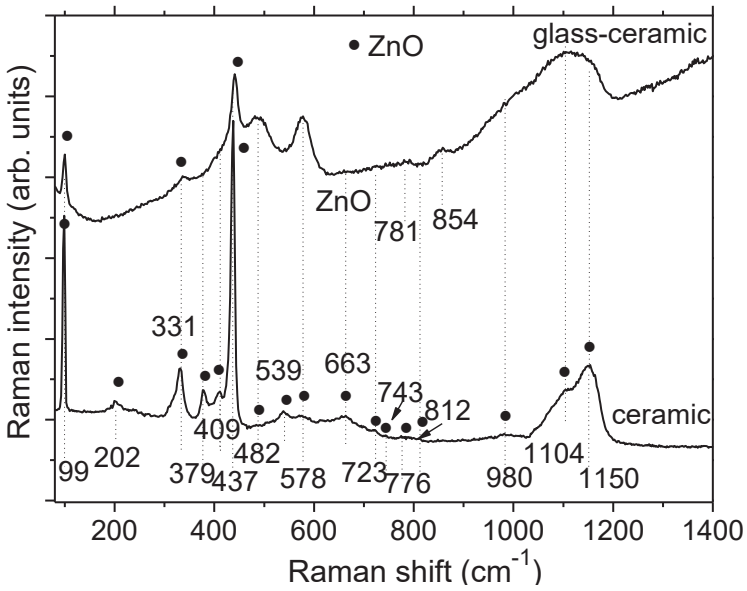

Figure 20. Raman spectra of the Zn2 glass-ceramics doped with 0.1 mol% Yb_2O_3 prepared by the heat-treatment at 750 °C for 2 h and of the ZnO:0.2 wt% Yb ceramic.

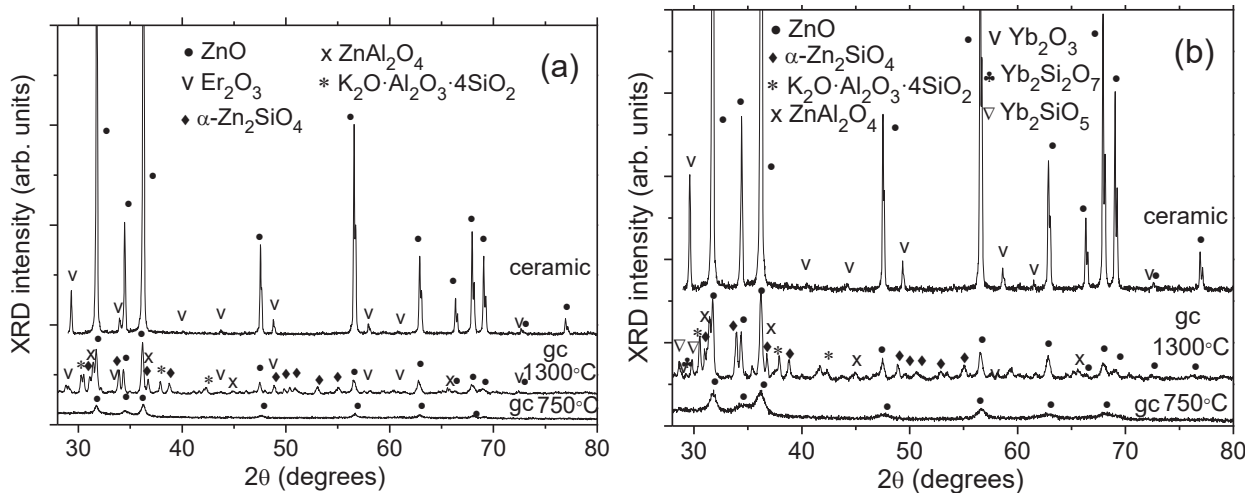

Figure 21. XRD patterns (a) of the Zn2 glass-ceramics doped with 1.5 mol% Er_2O_3 prepared by heat-treatments at 750 °C for 2 h and at 1300 °C for 2 h and of the ZnO:3 wt% Er ceramic; (b) of the Zn2 glass-ceramics doped with 1.5 mol% Yb_2O_3 prepared by heat-treatments at 750 °C for 2 h and at 1300 °C for 2 h and of the ZnO:3 wt% Yb ceramic.

Different origin of absorption peaks in spectra of glass-ceramics and ceramics doped with RE ions is revealed by the comparison of XRD patters and absorption peaks of Yb and Er-containing materials, see Fig. 22. Absorption spectra of ZnO:Yb and ZnO:Er ceramics are characteristic of corresponding RE oxides and demonstrate well-reserved multiplets. The broad peaks of RE ions in spectra of transparent glass-ceramic reflect their location in the residual glass phase.

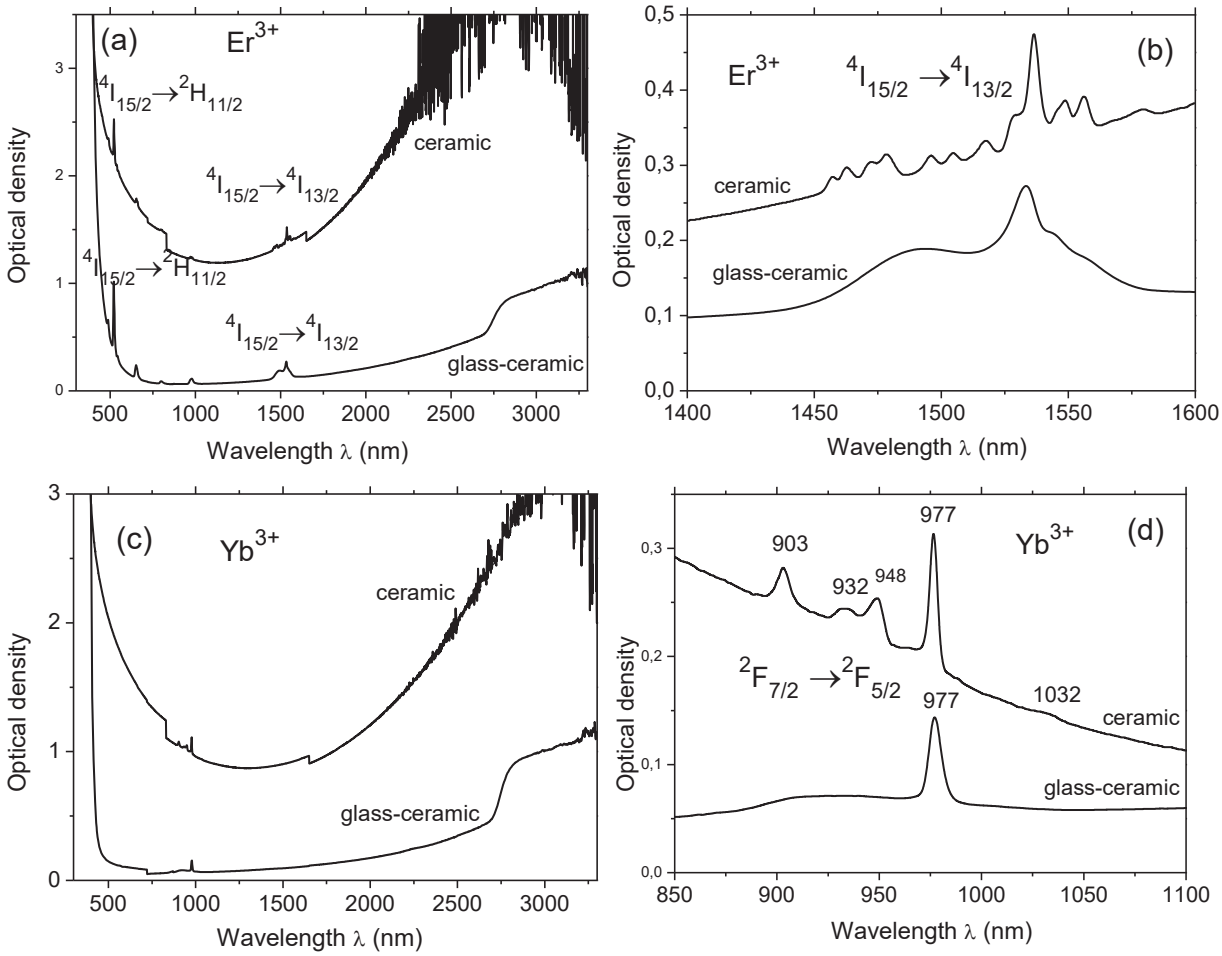

Figure 22. (a,b) Absorption spectra of the Zn2 glass-ceramics doped with 1.5 mol% Er_2O_3 prepared by the heat-treatment at 750 °C for 2 h and the ZnO:3 wt% Er ceramic in the spectral range of 300 – 3300 nm (a); in the spectral range of 1400 – 1600 nm (b). The thickness of the glass-ceramic sample is 1 mm, that of the ceramic sample is 0.5 mm. (c,d) Absorption spectra of the Zn2 glass-ceramics doped with 0.1 mol% Yb_2O_3 prepared by the heat-treatment at 680 °C for 48 h and the ZnO:3 wt% Yb ceramic in the spectral range of 300 – 3300 nm (c); in the spectral range of 850 – 1100 nm (d). The thickness of the glass-ceramic sample is 3 mm, that of the ceramic sample is 0.5 mm.

Conclusions

The structure and phase transformations in ZnO: glass-ceramics and optical ceramics doped with rare-earth and transition-metal ions were studied by small angle X-ray scattering, differential scanning calorimetry, X-ray diffraction analysis, transmission electron microscopy, and Raman spectroscopy. Morphology of the fracture surface of ceramics was characterized by scanning electron microscopy in combination with energy dispersive X-ray analysis. Absorption spectra of the materials were recorded.

It was revealed that during the initial glass casting and cooling, regions of structural inhomogeneity of various types are formed, depending on the type and concentration of the TM and RE ion. The character of the primary phase decomposition, which depends on the type and concentration of TM and RE ion, determines the kinetics of crystallization of ZnO and the time - temperature ranges of transformations of Zn-containing phases ZnO → β-willemite (β-Zn_2SiO_4)

→ α-willemite (α-Zn_2SiO_4) → ZnO+$ZnAl_2O_4$, observed with an increase in the heat-treatment temperature in the range of 680–1200 ºC.

In glass-ceramics, TM ions enter the ZnO and willemite nanocrystals. We demonstrated difficulty in incorporation of octahedrally coordinated TM ions into the structure of ZnO crystals.

RE ions do not enter the structure of ZnO crystals, but are located in the vicinity of these crystals and in the volume of the residual glass. As a result of high-temperature treatment, RE ions form their own phase of RE silicates. In the case of high concentrations of RE ions, RE_2O_3 crystals are formed as well.

The spectral-luminescent properties of transparent ZnO-based glass-ceramics are determined by the properties of both ZnO crystals and doping ions. Glass-ceramics prepared by heat-treatments at up to 900 ºC are usually transparent and contain either ZnO or a mixture of ZnO and β-willemite nanocrystals.

It was found that in optical ceramics, Co^{2+} ions enter the structure of ZnO crystals and form the CoO crystals while RE ions do not enter their structure, but are located both on the surface of the crystals and form their own phase of RE_2O_3. The CoO and RE oxides crystallinity fraction increases in proportion with the Co and RE ion doping level. Thus, ZnO optical ceramics doped with Co and RE ions cannot be considered single phase materials. Addition of RE ions leads to a significant decrease in the average size of ZnO crystals in ceramics from 40 to 5-15 μm. The texture characteristics of ZnO ceramics are changes with addition of RE ions, which implies modification of the surface of ZnO particles due to selective location of RE ions on certain grain boundaries.

The results obtained will be used in the development of novel transparent optical ceramics and glass-ceramics based on ZnO doped with RE and TM ions and characterized by low scattering losses, high luminescence efficiency and promising for a wide range of optoelectronic devices.

Acknowledgements

This work was partly supported by the RFBR (Grant 19-03-00855).

The authors express their gratitude to Dr. Maria Lukashova from Tescan Ltd in St. Petersburg for her assistance in the SEM-EDX study of the ZnO:Co ceramic.

References

1. M.S. Ramachandra Rao, T. Okada, ZnO nanocrystals and allied materials, Springer India 2014, 1374, ISSN 0933-033X ISSN 2196-2812 (electronic), ISBN 978-81-322-1159-4 ISBN 978-81-322-1160-0 (eBook), https://doi.org/10.1007/978-81-322-1160-0.

2. D. Daksh, Y.K. Agrawal, Rare earth-doped zinc oxide nanostructures: a review, Rev. Nanosci. Nanotechnol. 5 (2016) 1–27, https://doi.org/10.1166/rnn.2016.1071.

3. U. Orgur, Ya.I. Alivov, C. Liu, A. Teke, M.A. Reshnikov, S. Dogan, V. Avrutin, S.-J. Cho, H. Morkoc, A comprehensive review of ZnO materials and devices, J. Appl. Phys. 98 (2005) 041301(1–103), https://doi.org/10.1063/1.1992666.

4. L. Schmidt-Mende, J.L. MacManus-Driscoll, ZnO – nanostructures, defects, and devices, Mater. Today, 10(5) (2007) 40–48, https://doi.org/10.1016/S1369-7021(07)70078-0.

5. C. Klingshirn, J. Fallert, H. Zhou, J. Sartor, C. Thiele, F. Maier-Flaig, D. Schneider, H. Kalt, 65 years of ZnO research – old and very recent results, Phys. Status Solidi B 247 (2010) 1424–1447, https://doi.org/10.1002/pssb.200983195.

6. P.A. Rodnyi, I.V. Khodyuk, Optical and luminescence properties of zinc oxide, Opt. Spectrosc. 111 (2011) 776–785, https://doi.org/10.1134/S0030400X11120216.

7. B.K. Meyer, H. Alves, D.M. Hofmann, W. Kriegseis, D. Forster, F. Bertram, J. Christen, A. Hoffmann, M. Straßburg, M. Dworzak, U. Haboeck, A.V. Rodina, Bound exciton and donor–acceptor pair recombinations in ZnO, Phys. Status Solidi B 241 (2004) 231–260, https://doi.org/10.1002/pssb.200301962.

8. F. Rahman, Zinc oxide light-emitting diodes: a review, Opt. Eng. 58(1) (2019) 10901(1–20), https://doi.org/10.1117/1.OE.58.1.010901.

9. J. Theerthagiri, S. Salla, R.A. Senthil, P. Nithyadharseni, A. Madankumar, P. Arunachalam, T. Maiyalagan, H.-S. Kim, A review on ZnO nanostructured materials: energy, environmental and biological applications, Nanotechnol. 30 (2019) 392001(1–27), https://doi.org/10.1088/1361-6528/ab268a.

10 A. Kołodziejczak-Radzimska, T. Jesionowski, Zinc oxide - from synthesis to application: a review. Mater. 7(4) (2014) 2833–2881, https://doi.org/10.3390/ma7042833.

11. A. Sirelkhatim, S. Mahmud, A. Seeni, N.H.M. Kaus, L.C. Ann, S.K.M. Bakhori, H. Hasan, D. Mohamad, Review on zinc oxide nanoparticles: antibacterial activity and toxicity mechanism, Nano-Micro Lett. 7 (2015) 219–242, https://doi.org/10.1007/s40820-015-0040-x.

12. E.V. Kortounova, V.I. Lyutin, V.D. Dubovskaya, P.P. Chvanski, The growth of zinc oxide crystals with impurities, High Press. Res. 20(1–6) (2001) 175–183, https://doi.org/10.1080/08957950108206165.

13. L.N. Demianets, D.V. Kostomarov, I.P. Kuz'mina, S.V. Pushko, Mechanism of growth of ZnO single crystals, Crystallogr. Rep. 47 (2002) S86–S98, https://doi. org/10.1134/1.1529962.

14. V.A. Demidenko, E.I. Gorokhova, I.V. Khodyuk, O.A. Khristicha, S.B. Mikhrin, P.A. Rodnyi, Scintillation properties of ceramics based on zinc oxide, Radiat. Meas. 42 (2007) 549–552, https://doi.org/:10.1016/j.radmeas.2007.01.050.

15. J.S. Neal, D.M. DeVito, B.L. Armstrong, M. Hong, B. Kesanli, X. Yang, N.C. Giles, J.Y. Howe, J.O. Ramey, D.J. Wisniewski, M. Wisniewska, Z.A. Munir, L.A. Boatner, Investigation

of ZnO-based polycrystalline ceramic scintillators for use as α-particle detectors, IEEE Trans. Nucl. Sci. 56 (2009) 892–898, https://doi.org/10.1109/ TNS.2008.2004702.
16. M. Hong, D. Fredrick, D.M. Devito, J.Y. Howe, X. Yang, N.C. Giles, J.S. Neal, Z.A. Munir, Characterization of green-emitting translucent zinc oxide ceramics prepared via spark plasma sintering, Int. J. Appl. Ceram. Technol. 8 (2011) 725–733, https://doi.org/10.1111/j.1744-7402.2010.02527.x.
17. E.I. Gorokhova, P.A. Rodnyi, E.P. Lokshin, K.P. Lott, G.B. Kunshina, K.A. Chernenko, G.V. Ananieva, S.B. Eron'ko, I.V. Khodyuk, O.G. Gromov, E.A. Oreschenko, Structural, optical, and scintillation characteristics of ZnO ceramics, J. Opt. Technol. 78 (2011) 753–760, https://doi.org/10.1364/ JOT.78.000753.
18. M. Prakasam, O. Viraphong, D. Michau, A. Largeteau, Critical parameters to obtain Yb^{3+} doped Lu_2O_3 and ZnO transparent ceramics, Ceram. Intern. 40 (2014) 1859–1864, https://doi.org/10.1016/j.ceramint.2013.07.088.
19. G. Chen, M. Nikl, N. Solovieva, A. Beitlerova, J. Rao, Y. Yang, Y. Zhang, X. Jiang, C. Zhu, Photoluminescent properties of nanocrystallized zinc borosilicate glasses, Radiat. Meas. 38 (2004) 771–774, https://doi:10.1016/j.radmeas.2003.12.010.
20. M. Nikl, J. Pejchal, R. Jinhua, J. Zhang, G. Chen, A. Beitlerova, A. Yoshikawa, T. Fukuda, Photoluminescence of ZnO-aggregates in oxide glasses. Opt. Mater. 29(5) (2007) 552–555, https://doi.org/10.1016/j.optmat.2005.08.051.
21. L. Ding, Y. Yang, X. Jiang, C. Zhu, G. Chen, Photoluminescence of undoped and B-doped ZnO in silicate glasses, J. Non-Cryst. Solids 354 (2008) 1382–1385, https://doi.org/10.1016/j.jnoncrysol.2006.10.088.
22. G. Qian, X. Liang, J. Bei, S. Yuan, G. Chen, Photoluminescence properties of zinc oxide in barium and fluorine silicate glasses, J. Am. Ceram. Soc. 90(4) (2007) 1255–1257, https://doi.org/10.1111/j.1551-2916.2007.01594.x.
23. M. Cai, W. Mao, L. Calvez, J. Rocherulle, H. Ma, R. Lebullenger, X. Zhang, S. Xu, J. Zhang, Broadband blue emission from ZnO amorphous nanodomains in zinc phosphate oxynitride glass, Opt. Lett. 43(23) (2018) 5845–5848, https://doi.org/10.1364/OL.43.005845.
24. H. Masai, T. Toda, T. Ueno, Y. Takahashi, T. Fujiwara, ZnO glass-ceramics: An alternative way to produce semiconductor materials, Appl. Phys. Lett. 94 (2009) 151908(1–3), https://doi.org/10.1063/1.3120282.
25. H. Masai, T. Ueno, T. Toda, Y. Takahashi, T. Fujiwara, Processing and photoluminescence properties of surface crystallized ZnO glass-ceramics, J. Non-Cryst. Solids, 356(52–54) (2010) 3080–3084, https://doi.org/10.1016/j.jnoncrysol.2010.04.055.
26. H. Masai, T. Ueno, Y. Takahashi, T. Fujiwara, Precipitation of ZnO in Al_2O_3-doped zinc borate glass ceramics, Opt. Mater. 33(12) (2011) 1980–1983, https://doi.org/10.1016/j.optmat.2011.03.051.
27. H. Masai, T. Ueno, Y. Takahashi, T. Fujiwara, Correlation between surface-crystallized ZnO and the amount of Al_2O_3 in borate-based glass-ceramics, J. Amer. Ceram. Soc. 94(8) (2011) 2452–2457, https://doi.org/10.1111/j.1551-2916.2011.04604.x.
28. Y. Takahashi, M. Kinoshita, T. Miyazaki, M. Osada, N. Terakado, T. Fujiwara, Affects of supercooled liquid state on the properties of the crystallized phase: Microscopic and

spectroscopic observations in ZnO-crystallized glass-ceramics, Appl. Phys. Lett. 107 (2015) 061902(1–4), https://doi.org/10.1063/1.4928538.
29. L. Yang, X. Wang, Z. Li, P. Liu, F. Liu, S. Ge, F. Song, B. Liu, Y. Shi, R. Zhang, (Er, Yb)-co-doped multifunctional ZnO transparent hybrid materials: fabrication, luminescent and magnetic properties, J. Phys. D. Appl. Phys. 44 (2011) 155404(1–5), https://doi.org/10.1088/0022-3727/44/15/155404.
30. G. Singh, S. Kumar, V.P. Singh, R. Vaish, Transparent ZnO crystallized glass ceramics for photocatalytic and antibacterial applications, J. Appl. Phys. 125(17) (2019) 175102, https://doi.org/10.1063/1.5081988.
31. Z. Khalkhali, Z. Hamnabard, S.S.A. Qazvini, S. Baghshahi, A. Maghsoudipour, Preparation, phase formation and photoluminescence properties of ZnO–SiO_2–B_2O_3 glasses with different ZnO/B_2O_3 ratios, Opt. Mater. 34(5) (2012) 850–855, https://doi.org/10.1016/j.optmat.2011.11.020.
32. A. Bahadur, Y. Dwivedi, S.B. Rai, Structural and spectroscopic diagnosis of Eu:ZnO and Eu:Yb:ZnO glass and ceramics, Spectrochim. Acta A Mol. Biomol. Spectrosc. 91 (2012) 217–221, https://doi.org/10.1016/j.saa.2012.01.073.
33. O.M. Ntwaeaborwa, P.H. Holloway, Enhanced photoluminescence of Ce^{3+} induced by an energy transfer from ZnO nanoparticles encapsulated in SiO_2, Nanotechnol. 16 (2005) 865–868, https://iopscience.iop.org/article/10.1088/0957-4484/16/6/042.
34. J. Bang, H. Yang, P.H. Holloway, Enhanced luminescence of SiO_2 : Eu^{3+} by energy transfer from ZnO nanoparticles, J. Chem. Phys. 123 (2005) 084709(1–5), https://doi.org/10.1063/1.2007647.
35. Y. Yu, D. Chen, P. Huang, H. Lin, Y. Wang, Structure and luminescence of Eu^{3+} doped glass ceramics embedding ZnO quantum dots, Ceram. Int. 36(3) (2010) 1091–1094, https://doi.org/10.1016/j.ceramint.2009.12.007.
36. F. Xiao, R. Chen, Y.Q. Shen, Z.L. Dong, H.H. Wang, Q.Y. Zhang, H. D. Sun, Efficient energy transfer and enhanced infrared emission in Er-doped ZnO-SiO_2 composites, J. Phys. Chem. C 116 (2012) 13458−13462, https://doi.org/10.1021/jp304075g.
37. Y. Dimitriev, R. Iordanova, M. Milanova, A. Bachvarova-Nedelcheva, M. Hassan, M. Abdallah, Phys. Chem. Glas. – Eur. J. Glass Sci. Technol. B 53 (2012) 254–563, ISSN 00319090.
38. R. Nagai, T. Honma, T. Komatsu, Laser patterning of ZnO crystals on the surface of borosilicate glass, J. Am. Ceram. Soc. 93 (2010) 658–661, https://doi.org/10.1111/j.1551-2916.2009.03486.x.
39. C. Bae, K.-S. Lim, Enhanced blue emission in Er^{3+}/$Yb3^{3+}$ doped glass-ceramics containing Ag nanoparticles and ZnO nanocrystals, Curr. Opt. Photonics 3(2) (2019) 135–142, https://doi.org/10.3807/COPP.2019.3.2.135.
40. L.R. Pinckney, Transparent glass-ceramics based on ZnO crystals, Phys. Chem. Glass. – Eur. J. Glass Sci. Technol. B 47 (2006) 127–130, https://www.ingentaconnect.com/content/sgt/ejgst/2006/00000047/00000002/art00010.
41. W. Holand, G.H. Beall, Glass-Ceramic Technology, John Wiley & Sons, 2012.

42. Q. Luo, X. Qiao, X. Fan, X. Zhang, Near-infrared emission of Yb^{3+} through energy transfer from ZnO to Yb^{3+} in glass ceramic containing ZnO nanocrystals, Opt. Lett. 36 (2011) 2767–2769, https://doi.org/10.1364/OL.36.002767.
43. B. Ghaemi, G. Zhao, G. Jie, H. Xi, X. Li, J. Wang, G. Han, A study of formation and photoluminescence properties of ZnO quantum dot doped zinc-alumino-silicate glass ceramic, Opt. Mater. 33 (2011) 827–830, https://doi.org/10.1016/j.optmat.2011.01.009.
44. B. Ghaemi, G. Zhao, S. Huang, J. Wang, G. Han, Structural and luminescence properties of Er-doped zinc–alumino–silicate glass ceramic, J. Amer. Ceram. Soc. 95 (2012) 1911–1914, https://doi.org/10.1111/j.1551-2916.2012.05200.x.
45. J. Zhou, S. Peng, H.J. Qin, B. Ghaemi, B. Song, G.L. Zhao, J.X. Wang, G.R. Han, Fabrication and visible emissions of ZnO nanocrystal doped transparent zinc silicate glass-ceramics, J. Alloy. Compd. 776 (2019) 52–58. https://doi.org/10.1016/j.jallcom.2018.10.175.
46. I.P. Alekseeva, O.S. Dymshits, A.A. Zhilin, S.S. Zapalova, D.V. Shemchuk, Transparent glass–ceramics based on ZnO and ZnO:Co^{2+} nanocrystals, J. Opt. Technol. 81(12) (2014) 723–728, http://dx.doi.org/10.1364/JOT.81.000723.
47. G.M. Arzumanyan, E.A. Kuznetsov, A.A. Zhilin, O.S. Dymshits, D.V. Shemchuk, I. P. Alekseeva, A.V. Mudryi, V.D. Zhivulko, O.M. Borodavchenko, Photoluminescence of transparent glass-ceramics based on ZnO nanocrystals and co-doped with Eu^{3+}, Yb^{3+} ions, Opt. Mater. 62 (2016) 666–672, https://doi.org/10.1016/j.optmat.2016.10.054.
48. P. Loiko, O. Dymshits, A. Volokitina, I. Alekseeva, D. Shemchuk, M. Tsenter, A. Bachina, A. Khubetsov, E. Vilejshikova, P. Petrov, A. Baranov, A. Zhilin, Structural transformations and optical properties of glass-ceramics based on ZnO, β- and α-Zn_2SiO_4 nanocrystals and doped with Er_2O_3 and Yb_2O_3: Part I. The role of heat-treatment, J. Lumin. 202 (2018) 47–56, https://doi.org/10.1016/j.jlumin.2018.05.010.
49. M. Shepilov, O. Dymshits, I. Alekseeva, A. Hubetsov, D. Shemchuk, A. Zhilin, Structure and anomalous light scattering of Er-doped transparent glass-ceramics containing ZnO nanocrystals, J. Non-Cryst. Solids 571 (2021) 121067(1–10), https://doi.org/10.1016/j.jnoncrysol.2021.121067.
50. Q. Yang, L. Zhao, H. Yu, Q. Min, C. Chen, D. Zhou, X. Yu, J. Qiu, B. Li., X. Xu, UV-shielding device of high-stability glass embedded with in-situ growth of ZnO quantum dots, J. Alloys Compnd. 784 (2019) 535–540, https://doi.org/10.1016/j.jallcom.2019.01.078.
51. J. Zhou, B. Song, H. Qin, W. Lu, G. Zhao, Z. Huang, G. Han, Color-tunable and white emission of Tm^{3+} doped transparent zinc silicate glass-ceramics embedding ZnO nanocrystals, J Am Ceram Soc. 103 (2020) 1010–1017, https://doi.org/10.1111/jace.16775.
52. M. Duan, J. Wang, C. Liu, J. Xie, J. Han, Effects of SnO doping on the optical properties of ZnO in glass, J. Non-Cryst. Solids 459 (2017) 32–35, https://doi.org/10.1016/j.jnoncrysol.2016.12.024.
53. W. Lei, Z. Luo, Y. He, S. Liu, P. Zhang, H. Liang, A. Lu, Preparation and broadband white emission of Ce^{3+}-doped transparent glass-ceramics containing ZnO nanocrystals for WLEDs applications, J. Alloys Compd. 875 (2021) 159979(1–9), https://doi.org/10.1016/j.jallcom.2021.159979.

54. W. Lei, Z. Luo, Y. He, P. Zhang, S. Liu, A. Lu, ZrO_2-doped transparent glass-ceramics embedding ZnO nano-crystalline with enhanced defect emission for potential yellow-light emitter applications, Ceram. Int. 47 (2021) 35073–35080, https://doi.org/10.1016/j.ceramint.2021.09.049.
55. W. Lei, Z. Luo, H. Liang, Z. Zhou, C. Wen, Y. Wu, A. Lu, Enhanced defect emission of TiO_2-doped transparent glass-ceramics embedding ZnO quantum dots with optimized heat-treatment schedule, Ceram. Int. 48(4) (2022) 5609–5616, https://doi.org/10.1016/j.ceramint.2021.11.105.
56. X. Du, H. Zhang, C. Cheng, S. Zhou, F. Zhang, Y. Yu, G. Dong, J. Qiu, Space-selective precipitation of ZnO crystals in glass by using high repetition rate femtosecond laser irradiation, Opt. Express, 22 (2014) 17908(1–7), https://doi.org/10.1364/OE.22.017908.
57. C. Lin, J. Wang, X. Zhao, E. Zhu, N. Long, C. Rüssel, Competitive crystallization of β-Zn_2SiO_4 and ZnO in an aluminosilicate glass, Ceram. Int. 44 (2018) 7209–7213, https://doi.org/10.1016/j.ceramint.2018.01.168.
58. MAUD materials analysis using diffraction, a Rietveld extended program to perform the combined analysis, http://maud.radiographema.eu/.
59. L. Lutterotti, R. Ceccato, R. Dal Maschio, E. Pagani, Quantitative analysis of silicate glass in ceramic materials by the Rietveld method, Mater. Sci. Forum 278–281 (1998) 87–92, https://doi.org/10.4028/www.scientific.net/MSF.278-281.87
60. H. Lipson, H. Steeple, Interpretation of X-ray powder diffraction patterns, Macmillan, London, 1970.
61. J.A.R. Márquez, C.M.B. Rodríguez, C.M. Herrera, E.R. Rosas, O.Z. Angel, O.T. Pozos, Effect of surface morphology of ZnO electrodeposited on photocatalytic oxidation of methylene blue dye. Part I: Analytical study, Int. J. Electrochem. Sci. 6 (2011) 4059–4069.
62. V.N. Filipovich, Toward the theory of Small-Angle X-ray Scattering, Zh. Tekh. Fiz. 26(2) (1956) 398–416.
63. N.S. Andreev, V.N. Filipovich, O.V. Mazurin, E.A. Porai-Koshits, G.P. Roskova, Phase separation in glass, Elsevier Science Publishers B.V, Amsterdam, North-Holland, 1984, http://store.elsevier.com/Phase-Separation-in-Glass/isbn-9780080983653/.
64. M.P. Shepilov, O.S. Dymshits, A.A. Zhilin, S.S. Zapalova, On the measurements of scattering coefficient of nanostructured glass-ceramics by a serial spectrophotometer, Measurement 95 (2017) 306–316. http://dx.doi.org/10.1016/j.measurement.2016.10.014.
65. I. Alekseeva, O. Dymshits, M. Tsenter, A. Zhilin, V. Golubkov, I. Denisov, N. Skoptsov, A. Malyarevich, K. Yumashev, Optical applications of glass-ceramics, J. Non-Cryst. Solids 356 (52–54) (2010) 3042–3058, http://dx.doi.org/10.1016/j.jnoncrysol.2010.05.103.
66. P. Loiko, O. Dymshits, A. Volokitina, I. Alekseeva, D. Shemchuk, M. Tsenter, A. Bachina, A. Khubetsov, E. Vilejshikova, P. Petrov, A. Baranov, A. Zhilin, Structural transformations and optical properties of glass-ceramics based on ZnO, β- and α-Zn_2SiO_4 nanocrystals and doped with Er_2O_3 and Yb_2O_3: Part I. The role of heat-treatment, J. Lumin. 202 (2018) 47–56, https://doi.org/10.1016/j.jlumin.2018.05.010
67. P. MacMillan, B. Piriou, A. Navrotsky, A Raman spectroscopic study of glasses along the joins silica-calcium aluminate, silica-sodium aluminate, and silica-potassium aluminate,

Geochim. Cosmochim. Acta, 46 (11) (1982) 2021–2037, https://doi.org/10.1016/0016-7037(82)90182-X.
68. F.A. Seifert, B.O. Mysen, D. Virgo, Three dimensional network melt structure in the systems SiO_2-$NaAlO_2$, SiO_2-$CaAl_2O_4$ and SiO_2-$MgAl_2O_4$, Amer. Miner. 67 (7,8) (1982) 696–718.
69. D.W. Matson, S.K. Sarma, J.A. Fhilpotts, Raman spectra of some tecto silicates and of glasses along the orthoclase-anorthite and nepheline-anorthite joins, Am. Mineral. 71 (1986) 694–704.
70. C.A. Arguello, D.L. Rousseau, S.P.S. Porto, First-order Raman effect in wurtzite-type crystals, Phys. Rev. 181 (1969) 1351–1363, https://doi.org/10.1103/ PhysRev.181.1351.
71. P.A. Loiko, O.S. Dymshits, V.V. Vitkin, N.A. Skoptsov, A.A. Zhilin, D.V. Shemchuk, M.Ya. Tsenter, K.V. Bogdanov, A.M. Malyarevich, I.V. Glazunov, X. Mateos, K.V. Yumashev, Structure and nonlinear optical properties of novel transparent glass-ceramics based on Co^{2+}:ZnO nanocrystals, Laser Phys. Lett. 13 (2016) 055803 (7pp), https://doi.org/10.1088/1612-2011/13/5/055803.
72. P.A. Loiko, O.S. Dymshits, V.V. Vitkin, N.A. Skoptsov, A.A. Zhilin, D.V. Shemchuk, M.Ya. Tsenter, K.V. Bogdanov, A.M. Malyarevich, I.V. Glazunov, X. Mateos, K.V. Yumashev, Saturable absorber: transparent glass-ceramics based on a mixture of Co:β-Zn_2SiO_4 and Co:ZnO nanocrystals, Appl. Opt. 55(21) (2016) 5505–5512, http://dx.doi.org/10.1364/AO.55.005505.
73. N.N. Ovsyuk, S.V. Gorya, Amorphous-to-amorphous phase transition in zeolites, JETP Lett. 83 (2006) 109–112, https://doi.org/10.1134/S0021364006030064.
74. R. Pappalardo, D.L. Wood, R.C. Linares, Jr., Optical absorption study of Co-doped oxide systems. II, J. Chem. Phys. 35 (1961) 2041–2060, https://doi.org/10.1063/1.1732208.
75. Y.Z. Peng, T. Liew, W.D. Song, C.W. An, K.L. Teo, T.C. Chong, Structural and optical properties of Co-doped ZnO thin films, J. Supercond. 18 (2005) 97–103, https://doi.org/0.1007/s10948-005-2158-4.
76. S. Guo, X. Zhang, Y. Huang, Y. Li, Z. Du, Investigation on electronic structures and nature of charge-transfer transition of ZnO:Co with variation of Co content, Chem. Phys. Lett. 459 (2008) 82–84, https://doi.org/10.1016/j.cplett.2008.03.071.
77. L. Galoisy, G. Calas, Structural environment of nickel in silicate glass/melt systems: Part 1. Spectroscopic determination of coordination states, Geochim. Cosmochim. Acta 57 (1993) 3613–3626, https://doi.org/10.1016/0016-7037(93)90143-K.
78. R. Pappalardo, D.L. Wood, R.C. Linares, Optical absorption spectra of Ni doped oxide systems. I, J. Chem. Phys. 35(4) (1961) 1460–1480, http://dx.doi.org/10.1063/1.1732066.
79. M. Shepilov, O. Dymshits, I. Alekseeva, A. Hubetsov, D. Shemchuk, A. Zhilin, Structure and anomalous light scattering of Er-doped transparent glass-ceramics containing ZnO nanocrystals, J. Non-Cryst. Solids 571 (2021) 121067(1–10), https://doi.org/10.1016/j.jnoncrysol.2021.121067.
80. G.T. Chandrappa, S. Ghosh, K.C. Patil, Synthesis and properties of willemite, Zn_2SiO_4, and M^{2+}:Zn_2SiO_4 (M = Co and Ni), J. Mater. Syn. Proc. 7(5) (1999) 273–279.
81. O.S. Dymshits, A.A. Zhilin, T.I. Chuvaeva, M.P. Shepilov, Structural states of Ni(II) in glasses and glass-ceramic materials of the lithium-aluminium-silicate system J. Non-Cryst. Solids 127 (1991) 44–52, https://doi.org/10.1016/0022-3093(91)90399-Q.

82. D.L. Russell, K. Holliday, M. Grinberg, D.B. Hollis, Broadening of optical transitions in Cr^{3+}-doped aluminosilicate glasses, Phys. Rev. B 59(21) 13712–13718, https://doi.org/10.1103/PhysRevB.59.13712.
83. K. Tanaka, I. Yamaguchi, K. Hirao, N. Soga, Optical properties of transparent glass-ceramics containing $ZnGa_2O_4$: Cr^{3+} microcrystals, Bull. Inst. Chem. Res., Kyoto Univ., 72(2) (1994) 124–133.
84. B. Babu, V.P. Manjari, T. Aswani, G.T. Rao, R.J. Stella, R.V.S.S.N. Ravikumar, Structural, optical and magnetic properties of Cr^{3+} doped ZnO nanopowder, Indian J. Phys. 88(7) (2014) 683–690, https://doi.org/10.1007/s12648-014-0473-y.
85. B.C. Babu, G.-G. Wang, B. Yan, Q. Yang, A.P. Baker, Effects of Cr^{3+} addition on the structure and optical properties of α-Zn_2SiO_4 synthesized by sol-gel method, Ceram. Int. 44(1) (2018) 938–946, https://doi.org/10.1016/j.ceramint.2017.10.026.
86. W. Strek, P. Deren, B. Jezowska-Trzebiatowska, Optical properties of Cr^{3+} in $MgAl_2O_4$ spinel, Physica B, 152 (1988) 379–384.
87. W. Nie, F.M. Michel-Calendini, C. Linarès, G. Boulon, C. Daul, New results on optical properties and term-energy calculations in Cr^{3+}-doped $ZnAl_2O_4$, J. Lumin., 46(3) (1990) 177–190, https://doi.org/10.1016/0022-2313(90)90038-D.
88. E. Gorokhova, I. Venevtsev, I. Alekseeva, A. Khubetsov, O. Dymshits, L. Basyrova, E. Oreschenko, S. Eron'ko, F. Muktepavela, K. Kundzins, A. Zhilin, P. Loiko, Effect of Yb^{3+} doping level on the structure and spectroscopic properties of ZnO optical ceramics, J. Phys.: Conf. Ser. 2086 (2021) 012015(1–6), https://doi.org/10.1088/1742-6596/2086/1/012015.
89. E. Gorokhova, O. Dymshits, I. Venevtsev, L. Basyrova, I. Alekseeva, A. Khubetsov, M. Baranov, M. Tsenter, A. Zhilin, S. Eron'ko, E. Oreschenko, F. Muktepavela, K. Kundzins, P. Loiko, ZnO – Yb_2O_3 composite optical ceramics: Synthesis, structure and spectral-luminescent properties, J. Eur. Ceram. Soc., 42 (2) (2022) 616–630, https://doi.org/10.1016/j.jeurceramsoc.2021.10.031.
90. N.H. Perry, T.O. Mason, Phase equilibria of the zinc oxide–cobalt oxide system in air, 96(3) (2013) 966–971, https://doi.org/10.1111/jace.12103.
91. M.J. Sienko, R.A .Plane, R.E. Hester, Inorganic chemistry. Principles and elements, Cornell University, 1965, New York, Amsterdam, 188 p.
92. D. Barreca, C. Massignan, S. Daolio, M. Fabrizio, C. Piccirillo, L. Armelao, E.o Tondello, Composition and microstructure of cobalt oxide thin films obtained from a novel cobalt(II) precursor by chemical vapor deposition, Chem. Mater. 13(2) (2001) 588–593.
93. P. Loiko, A. Belyaev, O. Dymshits, I. Evdokimov, V. Vitkin, K. Volkova, M. Tsenter, A. Volokitina, M. Baranov, E. Vilejshikova, A. Baranov, A Zhilin, Synthesis, characterization and absorption saturation of Co:$ZnAl_2O_4$ (gahnite) transparent ceramic and glass-ceramics: a comparative study, J. Alloys Compd. 725 (2017) 998–1005, https://doi.org/10.1016/j.jallcom.2017.07.239.
94. L. Basyrova, V. Bukina, S. Balabanov, A. Belyaev, V. Drobotenko, O. Dymshits, I. Alekseeva, M. Tsenter, S. Zapalova, A. Khubetsov, A. Zhilin, A. Volokitina, V. Vitkin, X. Mateos, J.M. Serres, P. Camy, P. Loiko, Synthesis, structure and spectroscopy of Fe^{2+}:$MgAl_2O_4$

transparent ceramics and glass-ceramics, J. Lumin. 236 (2021) 118090 (1–17), https://doi.org/10.1016/j.jlumin.2021.118090.
95. R. Cusco, E. Alarcon-Llado, J. Ibanez, L. Artus, J. Jimenez, B. Wang, M. J. Callahan, Temperature dependence of Raman scattering in ZnO, Phys. Rev. B 75 (2007) 165202-1-11, https://doi.org/10.1103/PhysRevB.75.165202.